Microlenses fabricated by two-photon laser polymerization for intravital cell imaging with non-linear excitation microscopy

M. Marini[1,+], A. Nardini[3,+] , R. Martínez Vázquez[2,+], C. Conci[3], M. Bouzin[1], M. Collini[1], R. Osellame[2], G. Cerullo[4], B.S. Kariman[4], M. Farsari[5], E. Kabouraki[5], M.T. Raimondi[3,+,*] , G. Chirico[1,+,*].

1 Department of Physics, Università degli Studi di Milano-Bicocca, Piazza della Scienza 3, 20126, Milan, Italy
2 Institute for Photonics and Nanotechnologies (IFN), CNR, Piazza L. da Vinci 32, 20133 Milan, Italy
3 Department of Chemistry, Materials and Chemical Engineering "Giulio Natta", Politecnico di Milano, Piazza L. da Vinci 32, 20133 Milan, Italy
4 Department of Physics, Politecnico di Milano, Piazza L. da Vinci 32, 20133 Milan, Italy
5 FORTH/IESL, N. Plastira 100, 70013, Heraklion, Greece

+: contributed equally to the work
*: corresponding authors.

Keywords: 3D micro scaffolds, two-photon polymerization, microlenses, two-photon imaging, confocal microscopy, SZ2080.

Abstract.
Non-linear excitation microscopy offers several advantages for in-vivo imaging compared to conventional confocal techniques. However, tissue penetration can still be an issue due to scattering and spherical aberrations induced on focused beams by the tissue. The use of low numerical aperture objectives to pass through the outer layers of the skin, together with high dioptric power microlenses implanted in-vivo close to the observation volume, can be beneficial to the reduction of optical aberrations. Here, we develop and test on fibroblast cell culture plano-convex microlenses to be used for non-linear imaging of biological tissue. The microlenses can be used as single lenses or multiplexed in an array. A thorough test of the lenses wavefront is reported together with the modulation transfer function and wavefront profile. We could retrieve magnified fluorescence images through the microlenses coupled to commercial confocal and two-photon excitation scanning microscopes. The signal-to-noise ratio of the images is not substantially affected by the use of the microlenses and the magnification can be adjusted by changing the relative position of the microlens array to the microscope objective and the immersion medium. These results are opening the way to the application of implanted micro-optics for optical in-vivo inspection of biological processes.

1. Motivation/introduction

In vivo observation of tissue is desirable in many fields, from immunology[1,2] to the assessment of the foreign body reaction as a test of immunogenicity to biomaterials[3,4]. To date, different kinds of imaging windows have been developed and used[5] in combination with fluorescence microscopy. However, the majority of the existing optical windows influence and/or have a severe impact on the laboratory animal health and behavior, therefore limiting the medical relevance of the observations. We recently proposed a miniaturized (500 μm × 500 μm × 100 μm) imaging window, named Microatlas, which incorporates an array of micro-scaffolds, able to guide the regeneration of tissue at the interface with the implanted material[6]. Although the Microatlas has been validated up to now in embryonated chicken eggs[6], it can also be implanted sub cute in mice, in which case non-linear excitation microscopy would be the best choice for direct imaging. Non-linear excitation microscopy with near infrared (NIR) laser sources can mitigate the penetration issues in tissues[7,8] by reducing the effect of scattering on the point spread function. However, the reduction of scattering with wavelength is decreasing with a lower than fourth power law in animal tissues[9], and the spatial resolution of images in deep tissue is also limited by spherical aberrations. These beam aberrations arise simply from the propagation of the high numerical aperture beam through the different layers of the animal skin. Instead of imaging implanted scaffolds by means of the long working distance and high numerical aperture objective of an external microscope, our long-term purpose is to develop a set of microlenses that will be coupled directly to the micro scaffolds, implanted *in vivo*, and used to enable non-linear imaging of the tissue regenerated within the micro scaffolds, by focusing collimated beams right at the site of observation. Structuring of these microlenses directly on top of the micro scaffolds would then reduce the tissue-induced spherical aberrations and allow longitudinal studies of tissue regeneration *in vivo*. In order to image micro scaffolds extending ≈100 μm along the optical axis, we would need to fabricate microlenses with high curvature and smooth surface, and this is a particularly demanding task.

Among additive manufacturing (AM) techniques, the only suitable technology to achieve this goal is two-photon polymerization (2PP)[10–13].

In this framework, microlenses have already been developed and fabricated by 2PP, and tested for transmission imaging. From the very first study in this field[14], attention was drawn to the optimization of the optical quality of the surface, by reducing the fabrication thickness[15], or by changing the fabrication scanning path[14]. In this previous work, the microlenses, also in the form of an array, were tested for conventional transmission imaging. More recently, the optical characterization has encompassed the study of the Modulation Transfer Function (MTF), which is an indirect measure of the aberrations. For example, the group of Giessen[16] fabricated multi-microlens systems, and characterized them thoroughly for axial and non-axial aberrations. In a complementary study, the same group achieved the fabrication of free-form optical components directly on top of optical fibers for endoscopy[17]. In the same field of endoscopy, Li et al.[15] demonstrated the feasibility of 2PP of microlenses for optical coherence tomography (OCT) probes. However, to our knowledge, no attempt has been made to test microfabricated lenses under the more demanding signal/noise ratio conditions of fluorescence imaging or, even more demanding, in the case of non-linear excitation microscopy of biological samples.

The present work is specifically devoted to the design and simulation of microlenses for two-photon excitation microscopy, to the development of methods and protocols for their fabrication and to their experimental testing on cell imaging. We choose here 2PP to enable the fabrication of the microlenses surfaces with arbitrary shape at high resolution, and develop and test a scanning protocol that, based on a random polar scanning and a combination of laser and UV lamp polymerization, minimizes the surface roughness and simultaneously increases the fabrication throughput. We further fully characterize the microlenses for widefield transmission and fluorescence imaging and for confocal and two-photon scanning microscopy. These microlenses can be included in implantable devices for the direct

inspection of cellular dynamics *in vivo*[6] or in integrated in microfluidic setups for the *in vitro* monitoring of complex biosystems, such as organoids, directly in the organoid bioreactor.

2. Results and discussion

2.1 Microlenses design

The microlenses imply the use of collimated (or almost collimated) light. This is motivated by the rationale of this study, i.e. the use of a microlens or an array of microlenses right at the site of observation, typically an implanted micro scaffold, collecting and focusing a collimated beam.

The skin of a laboratory animal, like a rodent, is composed of several layers[18], partly made of muscle and partly of adipose tissue. Sebaceous glands and hair follicles, being obstacles larger than the light wavelength, give rise to complex diffraction patterns and also to beam attenuation. Instead, smaller components of the tissue give rise to diffuse scattering, whose effect on imaging can be reduced by adopting a recently developed heterodyne measurement and phase-conjugation correction of the scattered field[19,20]. Apart from these correction strategies, which are not the subject of this work, we notice that different skin layers are endowed with different refractive index values. In fact, the refractive index slightly changes among various tissues, being approximately equal to[9] $n \simeq$1.38-1.39 at $\lambda \simeq 630\,nm$ with the exception of adipose tissue that has $n \simeq 1.42$. The refractive index of the tissues decreases substantially with increasing wavelength[9] (**Fig.SI1**) according to a power law $\approx \lambda^{-1.5}$ over the range $400\,nm < \lambda < 700\,nm$, passing from $n \simeq$ 1.49 at $\lambda = 400\,nm$ to $n \simeq$ 1.40 at $\lambda = 700\,nm$. No data are available yet in the near infrared region typically used for non-linear excitation ($\lambda \geq 800\,nm$). However, from the data in ref. [9] we can estimate for the muscle $n \simeq$ 1.392 at $\lambda = 800\,nm$ (**Fig.SI1**). As a matter of fact, microlenses implanted subcute in mice will be probably embedded in the “panniculus carnosus”, similar to muscle, denser but with a lower refractive index than fat. All these considerations imply that the microlenses will be working in an environment having a refractive index about 30% higher than that of air, where

lenses are typically tested in optical studies. Therefore, larger curvature of the optical surfaces or even a larger refraction index should be used for the fabrication of our microlenses.

An example of the spherical aberrations observed with high numerical aperture optics in an inhomogeneous medium is simulated in **Fig. 1A**. The propagation medium is either pure water (refraction index $n_1 \simeq 1.34$ at $\lambda = 0.8\,\mu m$) or composed of two slabs of materials of thickness $8\,mm < d_1 < 10mm$ ($n_1 \simeq 1.34$) and $d_2 = f_{FFL} - d_1$ (with refractive index $n_2 = 1.45$; f_{FFL} is the front focal length). The test was performed on a plano-aspherical lens, 25.4 mm in size with curvature radius 12.6 mm (see **SI1** for details), optimized for propagation in water and a pupil size of 10 mm. The aberrations induced on the wavefront when increasing the pupil size and/or changing the composition of the propagation medium are primarily spherical and can be characterized by the Zernike polynomial[21] ${Z_4}^0$. The ${Z_4}^0$ amplitude, $a_{4,0}$, depends steeply on the pupil size for size larger than 10-15 mm (**Fig.1B**). The spherical aberration coefficient increases more steeply for the propagation in the inhomogeneous medium ($d_1 = 8\,mm$) than in pure water (**Fig.1B**) and arises from the mismatch in the refractive indices in the propagation medium as indicated by the linear dependence of $a_{4,0}$ on the refractive index n_2 (**Fig.1A**) and on the thickness d_2 of the high refractive index slab (**Fig.1B**, inset). The possibility to obtain the tight focusing of a Gaussian laser beam needed for non-linear excitation microscopy is therefore limited by the propagation in inhomogeneous media. This drawback can be overcome by the use of microlenses implanted close to the observation field.

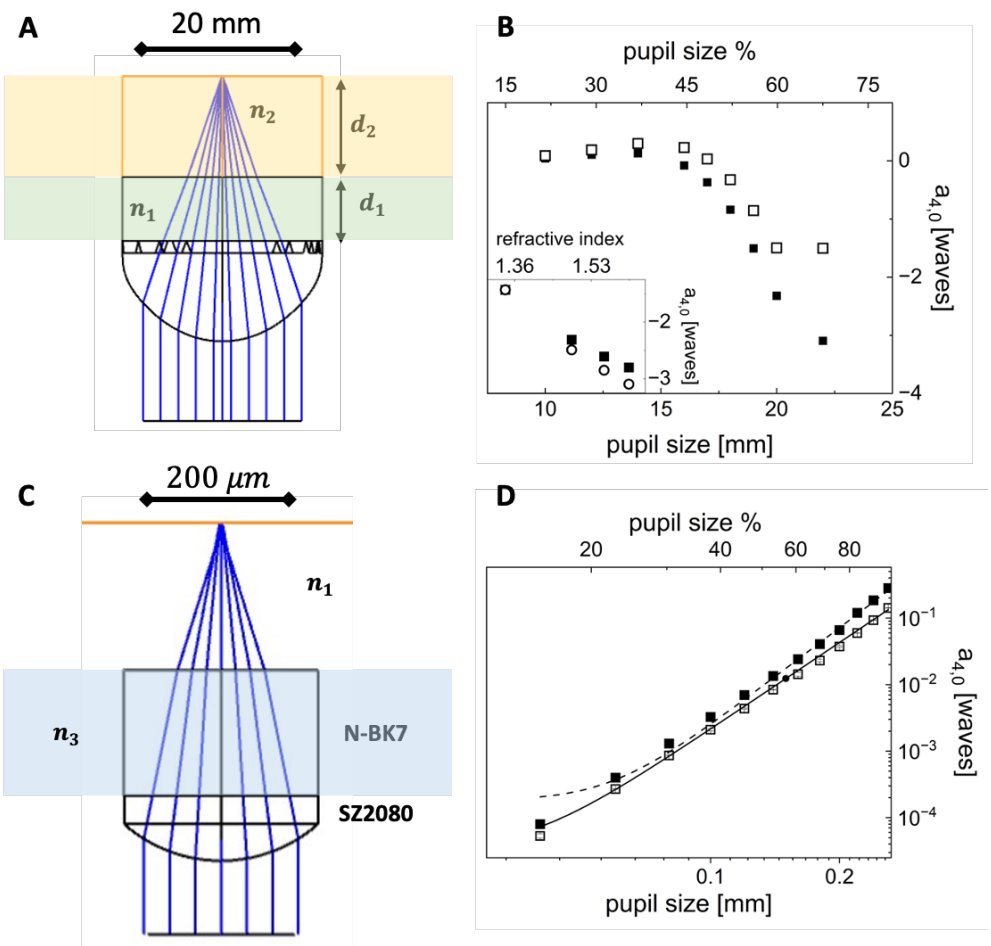

Figure 1. Simulation of the spherical aberrations arising on highly collimated beams when passing through an inhomogeneous sample ($\lambda = 0.8\ \mu m$). **A:** sketch of a macroscopic plano-aspherical lens working in an inhomogeneous medium (refractive indices are $n_1 = 1.34$ and $n_2 = 1.45$, $8mm < d_1 < 10\ mm, d_2 = f_{FFL} - d_1$). **B**: spherical aberration coefficient $a_{4,0}$ for the lens in panel **A** as a function of the pupil size for propagation in homogeneous (open squares) or inhomogeneous medium (filled squares, d_1 = 8 mm). Inset: dependence of $a_{4,0}$ as a function of the n_2 refractive index ($d_1 = 8mm$ open squares; $d_1 = 10mm$ filled squares). **C**: diagram of a single plano-convex microlens (diameter = 264 μm) fabricated on a N-BK7 glass substrate ($170\ \mu m <$ thickness $< 230\ \mu m$). Tissue is approximated with sea water ($n_1 = 1.34$). **D**: spherical coefficient $a_{4,0}$ for the lens in panel **C** as a function of the microlens pupil size, p, in air (filled squares) and in water (open squares). The solid and the dashed lines are the best fit to the data to a power law $a_{4,0} \propto p^{-4.3\pm0.3}$.

Aiming at the development of methods and protocols for rapid prototyping of microlenses with the optical quality needed to prime non-linear excitation, we focus here on the simplest case of a refractive lens, i.e. a plano-convex lens with a pedestal, fabricated on top of a supporting borosilicate glass slide (thickness $\simeq 170\ \mu m$, **Table I**). The plano-convex lens is a good approximation of the shape that theoretically minimizes the spherical aberrations for collimated

light[22]. The geometrical design parameters of the lens are reported in **Table I** together with a sketch of the microlens and the location of its principal planes.

Table I: geometrical parameters of the plano-convex microlens.

surface	curvature radius $[\mu m]$	thickness $[\mu m]$	material	refractive index $[\lambda = 0.8\ \mu m]$	radius $[\mu m]$	sketch
1	200.0	50.0	SZ2080	n= 1.46*	132.0	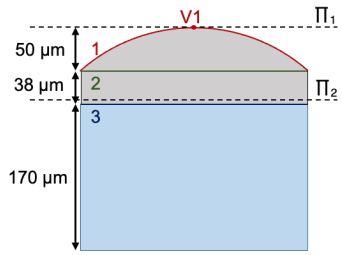
2	∞	38.0	SZ2080	n= 1.46*	132.0	
3	∞	170.0	N-BK7	n= 1.52	132.0	

Geometrical parameters for a plano-convex lens microfabricated in SZ2080. The effective front focal length in air is $f_{FFL} \simeq 164\ \mu m$. The two principal planes (Π, dashed lines in the sketch) lie at the vertex V1 and $35\ \mu m$ below surface 2. *from ref. [23].

An example of the design of a plano-convex microlens with diameter 264 µm is reported in **Fig.1C** for axial illumination. This microlens allows wide-field imaging with a field of view of ≃ 250 µm (see **SI5, "Field of view of microlenses"**). In order to image wider fields of view, these microlenses could be assembled in a microarray.

The beam focused by the microlens is slightly aberrated even by using the maximum pupil size $\simeq 260\ \mu m$, as can be judged from the intensity profile of a Gaussian beam simulated at the microlens focal plane (**Fig.SI2.2B**) where we can estimate a beam waist ($1/e^2$ radius) of $(1.20\ \pm 0.03)\ \mu m$ at $\lambda = 0.8\ \mu m$ (**Fig.SI2.2**), a value only 2-3 times larger than the one typically used for two-photon excitation in biological samples. The aberrations on the wavefront can be quantified at the focal plane of the microlens (the plane of the circle of minimum confusion) in terms of the Zernike polynomials: we find again that the major contribution for axial propagation is the spherical one corresponding to the Zernike polynomial[21] ${Z_4}^0$. The $a_{4,0}$ coefficient increases steeply as a power law with exponent $\simeq 4$ (**Fig.1D**), as expected for the thin lens treatment[22]. The spherical aberrations resulted slightly larger when the microlens

is focusing in air (**Fig.1D**, filled symbols) rather than in water (**Fig.1D**, open symbols), due to index matching at the exit pupil.

2.2 Fabrication and characterization by scanning electron microscopy (SEM)

Following the simulations reported in the previous section, we decided to fabricate plano-convex lenses by 2PP of the SZ2080 photoresist, a biocompatible photosensible material[23]. Single plano-convex lenses, or a hexagonal microarray of these microlenses, were fabricated on top of a supporting borosilicate glass with a thickness of 170 μm that is integral to the design of the system. Each microlens has the geometrical parameters reported in **Table I**.

2PP is intrinsically a slow fabrication method. In fact, 2PP structuring of the whole volume of a full microlens requires up to 12 hours. Therefore, we had two major requirements: first of all to speed up the production, and then to obtain an optical quality surface. In order to speed up the process and to match a reasonable prototyping time, we decided to two-photon polymerize the outer surface of each lens only (**Fig.2A**), and to subsequently expose to UV radiation the sample, in order to crosslink the unpolymerized photoresist within the volume by a bulk one-photon polymerization (**Fig.2B**).[14,24–26] In addition, in order to provide high surface quality, the polymerization of the contour was carried out by a concentric circular scanning of the impinging laser beam around the lens axis (**Fig.2C**). Starting from the CAD design of the lens from Zemax calculations, we used a dedicated code to slice the model and to obtain a matrix of points in cartesian coordinates for each slicing plane. The G-code for the microfabrication has been defined as a sequence of concentric circles with a decreasing radius along the optical axis of the lens (**Fig.2C**). To smooth the outer surface, a good superposition of the polymerized circles has been obtained managing both the vertical step $\delta Z_{slicing}$ (typically $\delta Z_{slicing} <= 1\ \mu m$) and the planar step δR_{Raster} as the radius of each cycle ($\delta R_{Raster} <= 0.5\ \mu m$) relative to the curvature of the spherical surface (**Fig.2D**).

The fabrication process was carefully optimized to obtain the smoothest surface for the microlenses. In the first outcomes of fabrication, the spherical outer surface was affected by a visible hinge related to the start and end points of each polymerized circle (**Fig.2E-F**). Accordingly, we implemented in the code a random distribution of the start/end writing points within an angle of 120 degrees. The homogeneity of the outer surface increased, despite a few regions of overexposure related to the writing acceleration and deceleration during the rotations (**Fig.2G-H**). To avoid this effect, we added a rotation without irradiating the photoresist before and after each polymerization cycle. The quality and the smoothness of the outer surface is visibly improved, even if the central region on the top plane of the lens is still affected by the very dense overlap of the polymerized lines resulting in an overexposed region. Therefore, according to the planar and vertical resolutions of the polymerization voxel, which are XY_{Voxel} ~ 1 μm and Z_{Voxel} ~ 5 μm respectively, the fabrication protocol was optimized by excluding a central area of the top of the lens with radius ~ 1 μm from the 2PP process. Still, some effect of the overexposure was present (**Fig.2H**). As literature evidence demonstrates, the complete homogeneity of the central part is a common and crucial issue related to the technique and the process of fabrication.[25] The top area polymerization was then optimized by slowly reducing the translation speed and laser power (1-2% in each step) in the last 2PP loops.[27]

After the two-photon polymerization of the outer surface of the microlens, the surrounding unpolymerized photoresist was removed and then the core of the lens was cured by UV irradiation (Materials and Methods section).

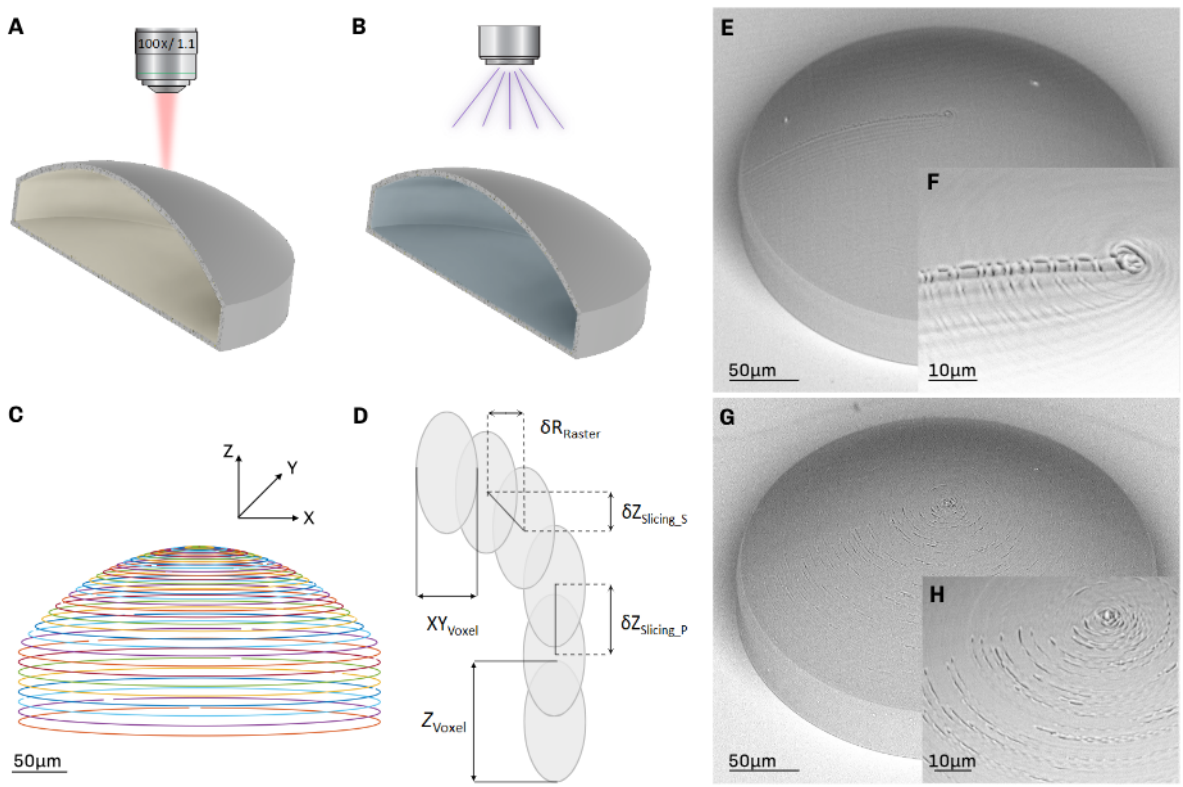

Figure 2. Scheme of the microlens fabrication protocol. **A**: 2PP of the lens outer surface focusing the laser beam with a 100x water immersion objective (NA 1.1). **B**: UV exposure to crosslink the unpolymerized core of the lens. **C**: rendering of the outer shell of the microfabricated lens obtained from the G-code as a sequence of concentric cycles with decreasing radius along the optical axis of the lens. **D**: details of the contour parameters of rasterization and slicing on both the pedestal ($\delta Z_{Slicing_P}$) and spheric ($\delta Z_{Slicing_S}$, $\delta R_{_Raster}$) part of the lens, and three-dimensional resolution of the polymerization voxel (XY_{voxel}, Z_{voxel}). **E**: SEM image of the deterministic polar scanning (non-random distribution of the start/end writing points). **F**: detail of the hinge on the outer surface due to the same start Y coordinate at each rotation. **G**: SEM image of a microlens after the randomization of the distribution of the start/end points for each rotation. **H**: detail of the overexposure effect due to the acceleration and deceleration of the translation stages during laser irradiation (random start-end point within an angle of 120 degrees).

In summary, the optimized fabrication protocol promotes a 98% reduction of the fabrication time, if compared to the one required to 2PP the whole volume of a full lens (from 12 hours to 8 minutes). At the same time, both slicing and radial steps, here employed, ($\delta Z_{slicing} = 1\ \mu m$; $\delta R_{Raster} = 0.5\ \mu m$) both the fabrication protocol we devised, allowed us to obtain a lens surface quality appropriate to perform optical imaging (as better shown in the optical characterization section) and with a good reproducibility ($\pm 5\%$) of the shape (see **SI 6,**

"Profilometer analysis of the shape of the microlenses"). In addition, an even smoother surface can be obtained, by decreasing the imposed radial step to $\delta R_{Raster} \simeq 0.3\ \mu m$, during the polymerization at the expense of the fabrication time. Fabrication time increases from 8 minutes per lens at $\delta R_{Raster} \simeq 0.5\ \mu m$ to 15 minutes per lens at $\delta R_{Raster} \simeq 0.3\ \mu m$. Overall, we obtain stable microlenses with optical quality and with a higher size if compared with the microlenses fabricated by 2PP in the literature.[14,16,24,25,28–30]

Our imaging area can be even increased with respect to the predicted $\simeq 250\ \mu m$ for a single microlens (**SI5, "Field of view of microlenses"**) by rescaling the microfabrication process to an hexagonal array of microlenses covering an area of $\simeq 800\ \mu m$ (**Fig.3B**). Four hexagonal arrays (**Fig.3C**) were fabricated on a 12mm Ø circular glass substrate (170 µm thickness) covering an area 1.5 mm in side. The production of one set of arrays requires less than 4 hours.

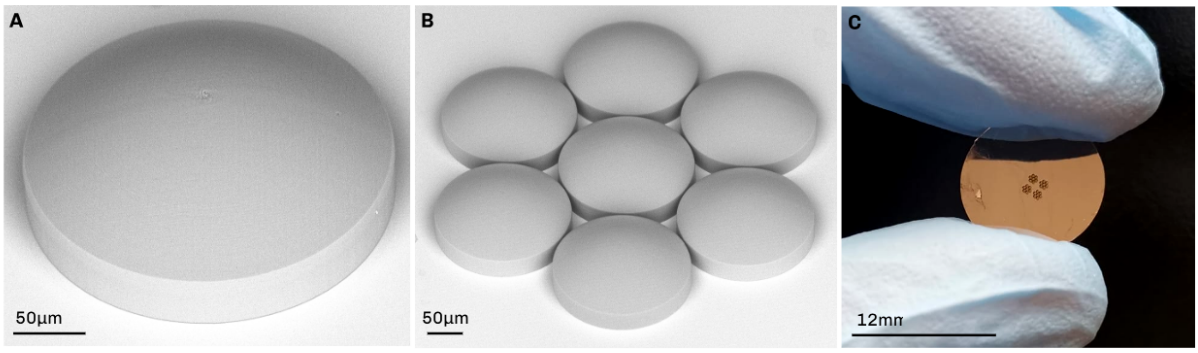

Figure 3. Final outcome of fabrication. **A**: SEM image of one microlens obtained from the optimization of the 2PP fabrication process and UV exposure. **B**: SEM image of one array of seven microlenses symmetrically set in a hexagonal configuration covering an area 800 µm in diameter. **C**: Image of a sample with 4 arrays of seven microlenses each covering an area 1.5 mm in side.

2.3 Optical characterization.

Before assessing the possibility to get fluorescence images of cells through the fabricated microlenses, we tested their optical quality by the study of the intensity distribution of a beam propagating along the optical axis, the wavefront measurement at the focal plane and the

measurement of the modulation transfer function. For all these tests, we used a collimated diode laser beam at $\lambda = 635\, nm$.

Minimum spot size under collimated beam. The intensity distribution on planes perpendicular to the optical axis provides a direct visualization of the effect of the aberrations, each having a peculiar signature.[31] The microlenses were tested in overfilling conditions to enhance the aberration effect. The intensity distributions sampled at $10\, \mu m$ steps (**Fig.4A** and **SI7, "Intensity distribution sampling along the optical axis"**) in a range of about $\pm 20\, \mu m$ around the effective focal plane of the microlens (corresponding to the minimum spot size) are reported in **Fig. 4B**. These images indicate the presence of spherical aberrations as concentric circles, turning more evident for distances $z < f_{FFL}$: for planes at distances larger than the front focal length, $z > f_{FFL}$, as expected,[31] the central peak of the intensity distributions becomes more diffuse and the concentric rings cannot be singled out. The simulated intensity distributions (**Fig.4C**) agree with the experimental ones. Due to the presence of the spherical aberration rings, we cannot define a Gaussian width ($1/e^2$) for the intensity distribution across the optical axis (see **SI7, "Intensity distribution sampling along the optical axis"**).[32] However, the full width at half maximum (FWHM) of the central spot in planes close to the plane of minimum confusion can be measured on cross-section profiles of the intensity distributions. The full width, FWHM $= 0.98 \pm 0.10\, \mu m$ (averaged over an entire array of 7 microlenses), is in very good agreement with the simulation of the beam profile (**Fig.4D**). This value corresponds to a beam waist ($1/e^2$ radius) $w_0 = 0.84 \pm 0.09\, \mu m$. An estimate of the Rayleigh range, z_R, can be obtained by the relation $z_R = \pi {w^4}_0 / \lambda \simeq 2.5 \pm 1.1\, \mu m$.

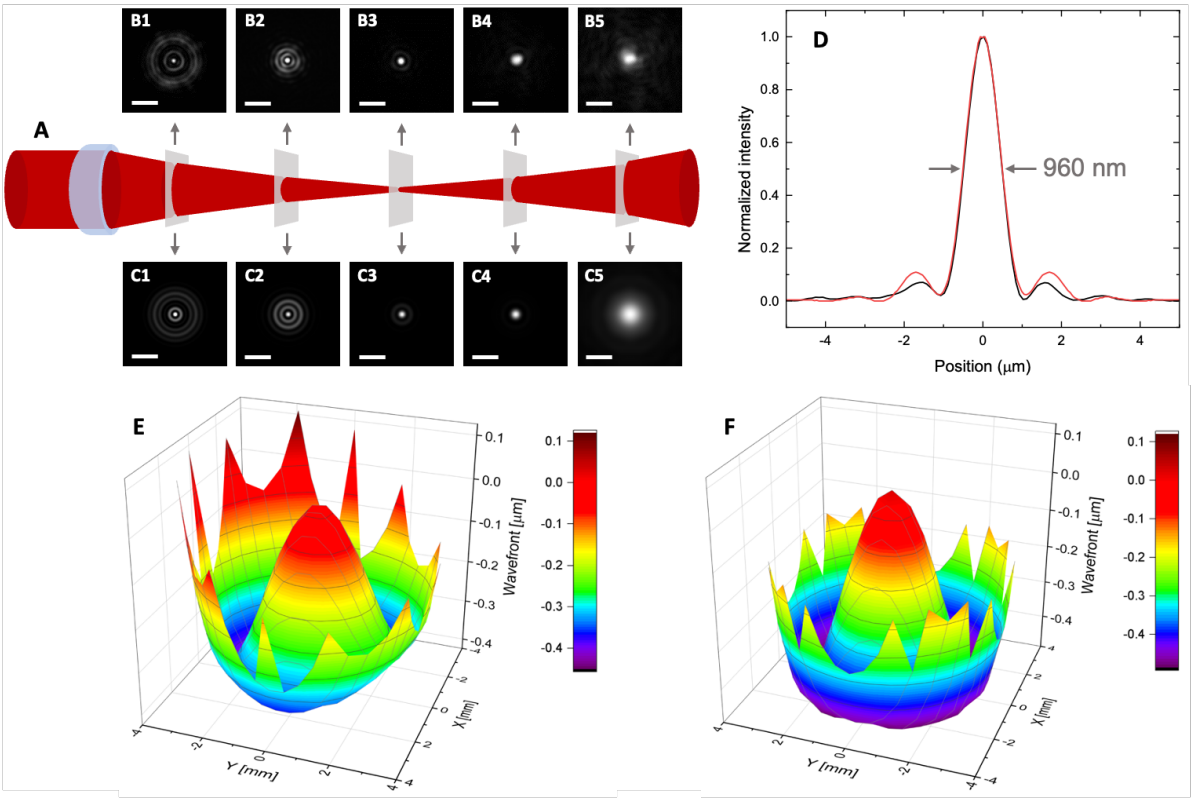

Figure 4. Aberrations of the microlenses. **A**: Schematics of the configuration adopted for the measurement of the intensity distribution of a Gaussian beam focused by a plano-convex microlens (**Table I**). The tube lens and the camera sensor are aligned to accept rays from infinite (see **Fig.SI7** for details). **B**: Images of the intensity profiles collected at various distances along the optical axis. The mutual distance between the planes is 10 μm, starting from the plane closer to the microlens (from left to right). Scale bars 5 μm. **C**: Simulated intensity distributions with the same 10-μm spacing along the optical axis. Scale bars 5 μm. **D**: Exemplary profile of a Gaussian beam focused by one microlens (the beam overfills the microlens). Experimental and simulated data are reported as black and red lines, respectively. The FWHM of the experimental profile is $FWHM \simeq 960\ nm$. **E-F**: Measured (**E**) and simulated (**F**) wavefront at the focal plane (minimum confusion plane) of the microlens. Piston, tip and tilt aberrations were subtracted from the experimental wavefront for visualization.

<u>Wavefront measurement.</u> The wavefront was measured by means of a Shack-Hartman sensor (**SI4**, "**Microlens wavefront measurement**"). The resulting wavefront of the microlens, at the maximum pupil of about $264\ \mu m$ is reported in **Fig.4E**. The mexican-hat shape is typical of the ${Z_4}^0$ Zernike polynomial that characterizes the first-order spherical aberration. In fact, the Zernike decomposition of the experimental wavefront gives an amplitude of the spherical component $a_{4,0} = 0.10\ \pm 0.01\ \mu m$ (averaged over an entire array of microlenses), whereas all the other Zernike coefficients are lower than $0.02\ \mu m$. The wavefront predicted for the microlens by Zemax simulations, reported in **Fig. 4F**, agrees in shape with the experimental

one. The predicted value $a_{4,0}{}^{(Z)} = 0.15\ \mu m$ is larger than the measured value $a_{4,0}$. Indeed, while the simulated distribution of the Zernike weights is peaked on a specific aberration component (here, the spherical one), the experimental wavefront is described by a distribution of Zernike polynomials: together with the dominant spherical component, $a_{4,0}$, other aberrations contribute with small, but non-zero, coefficients. As a consequence of the superposition of multiple aberration coefficients, the fit of the resulting experimental wavefront to the Zernike polynomials results in an effectively higher uncertainty on $a_{4,0}$. This is probably the origin of the discrepancy between the numerical values of $a_{4,0}{}^{(Z)}$ and $a_{4,0}$.

Still, the peak-to-valley (or Root-Mean-Square, RMS) wavefront error determines the overall optical quality more prominently than the amplitude of individual Zernike coefficients. Indeed, the average peak-to-valley wavefront distortion, after subtraction of the piston, tip and tilt components, is about $0.62 \pm 0.04\ \mu m$ and it is similar to the simulated value (**Fig.4F**) of $0.51\ \mu m$. Analogously, the average RMS value is $0.13 \pm 0.02\ \mu m$ and is in good agreement with the Zemax prediction, RMS $= 0.15\ \mu m$.

Overall, the $a_{4,0}$ and RMS wavefront error of the microlens reveal an even better behavior of the microlens when compared to a commercial macroscopic plano-convex lens (f = 25mm, Thorlabs, LA1252) with ~35% pupil size (see **SI4**, **"Microlens wavefront measurement"**).

<u>Modulation transfer function.</u> The MTF can be measured pointwise by means of the analysis of a reference target, such as the USAF 1951. A qualitative result of the imaging of the USAF target through the microlenses is given in **Fig.5A-B**. The microlenses are used in a finite conjugate condition (**Fig.5H** and **Fig.SI3.1A**), with a magnification determined by the ratio of the distance (q) between the image plane and the exit principal plane over the distance (p) between the sample plane and the entrance principal plane. A 20x microscope objective collects the image produced by the microlens in the objective focal plane.

The MTF of the fabricated microlenses was derived by inserting a sharp edge in the sample plane, and by collecting and digitizing an image to retrieve the Edge Spread Function (ESF) (**Fig.5C,D**). We computed the derivative of the ESF to obtain the Line Spread Function (LSF),

whose Fourier transform is the Modulation Transfer Function (MTF, **Fig.5D**). The MTF, that is the modulus of the Fourier Transform of the point spread function, offers a complete evaluation of the optical response of the microlenses for imaging purposes.[33] A 10% modulation is reached at a cutoff frequency of about 490 lines pairs/mm, which is comparable to the cutoff frequency of more sophisticated microfabricated optics in the recent literature.[16]

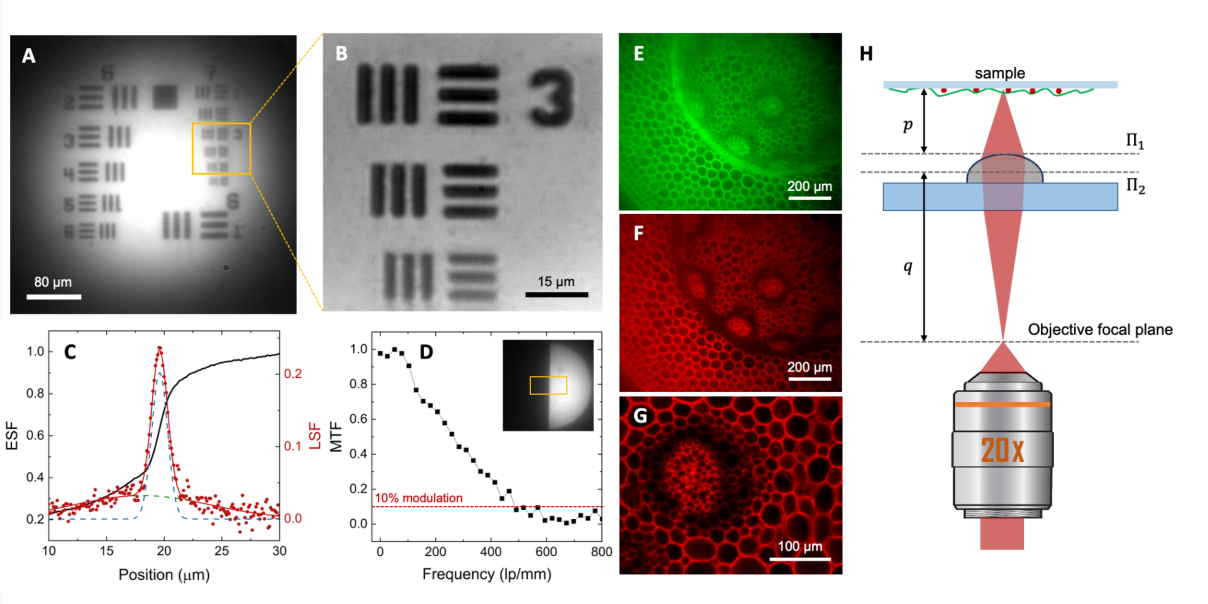

Figure 5. Optical performance of the microlenses. **A-B**: Example of widefield images of an USAF1951 resolution test chart obtained by a single microlens and a 20x objective as described in the text. Depending on the adopted relative positions of the microlens and the objective the overall magnification equals 6x (**A**) and 30x (**B**). **C-D**: Measurement of the MTF (Modulation Transfer Function) of the microlenses by the knife edge method. **C**: Edge Spread Function (ESF, black solid line) and Line Spread Function (LSF, red circles) of a single microlens. In order to eliminate the background contribution, the LSF is fitted to a two-component Gaussian function (dashed lines), the background wider Gaussian component is subtracted, and the resulting LSF is Fourier transformed to retrieve the MTF. **D**: MTF of the microlens derived as the Fourier transform of the background-subtracted LSF in panel **C**. Inset: Image of a sharp razor blade produced by the microlens and exploited for the ESF quantification. The ESF is extracted as the average intensity profile along the horizontal axis within the yellow Region of Interest; the LSF is computed as the first derivative of the ESF. **E-F**: Widefield images of a sample of Convallaria Majalis obtained under blue (E) and green (F) excitation and epifluorescence collection. **G:** Control image of the same sample obtained on a widefield microscope (Materials and Methods section). **H**: sketch of the finite conjugate use of the microlens. Π_1 and Π_2 are the two principal planes.

<u>Cell imaging through the microlenses.</u> As a proof of concept, microlenses can be coupled to a widefield microscope to collect widefield images both in transmission and in fluorescence mode, or can be coupled in a virtual image configuration to a scanning optical microscope

371 (see **SI3, "Microlens coupled to a raster scanning optical microscope"**). In the first case,
372 the microlenses are used in the same finite conjugate condition (**Fig.5H** and **SI3**) exploited for
373 the USAF target imaging in **Fig.5**. Examples of fluorescence widefield images collected in this
374 configuration are reported in **Fig.5E,F** for a sample of Convallaria Majalis, excited in the blue
375 (**Fig.5E**) or the green (**Fig.5F**) spectral bands. From these images, very similar to the ones
376 obtained using a widefield microscope **(Fig.5G**), we can clearly distinguish the most relevant
377 parts of the root. The pericycle and endodermis appear as a bright green circle in **Fig. 5E**,
378 surrounding a set of xylems and phloems and surrounded by the cortex. A slight field curvature
379 can be observed at the edge of the field of view in **Figs.5E** and **5F**, compared to the reference
380 image in **Fig.5G**.
381 For non-linear excitation microscopy it is essential to couple the microlens with a scanning
382 setup. In this second type of application, we couple the microlenses directly to a low numerical
383 aperture objective in a raster scanning optical microscope. The microlens is set at a distance
384 from the exit lens of the objective smaller than the objective working distance (see **Fig.6J** and
385 **SI3**, **"Microlenses coupled to a raster scanning optical microscope"**). In this configuration
386 the microlens creates, for any position of the laser beam during the scanning, a virtual image
387 of the sample that is then collected by the microscope objective. The magnification of the
388 resulting image can be computed as the product of the magnification of the objective and that
389 of the microlens. The latter depends directly on the distance, δz, between the microlens and
390 the sample plane of the microscope objective (for details see **SI3,** "**Microlenses coupled to**
391 **a raster scanning optical microscope**"). This configuration can be implemented both on
392 confocal and on non-linear excitation fluorescence microscopes, also in the case of a
393 microlens array, as reported in **Fig.6**. In the example of **Fig.6**, the sample is a cell culture
394 (human dermal fibroblasts) grown on the very same glass slide (opposite side) where the
395 microlenses are fabricated. Fibroblasts can be imaged by the microlenses by properly
396 adjusting the position of the microlens array with respect to the microscope objective. When
397 $\delta z \simeq 0$, only the cells not covered by the microlenses get imaged, with the microscope
398 objective magnification (**Fig.6A** and **Fig.6D**). When $\delta z \simeq 165\ \mu m$, one can get images of the

cells through the microlenses (**Fig.6B,C**). The estimated transverse magnification due to the microlens (see **SI3, "Microlenses coupled to a raster scanning optical microscope**") is $M_T \simeq 2.4$. 3D reconstruction of the cell culture is possible too, as shown in **Fig.6E**.

Notably, the resolution and the signal to noise ratio of the images collected through the microlenses are very similar to the ones obtained on the confocal microscope in its conventional configuration. Moreover, we can verify that the microlenses optical quality is sufficient to induce two-photon excitation and to collect non-linear excitation fluorescence images both when used in air (**Fig.6F**) and when used with water immersion objectives (**Fig.6H**), despite the lower dioptric power of the microlenses, due to partial index matching. When the microlenses are coupled with a 20X dry microscope objective we found that the images of the cells through the microlenses can be recovered at $\delta z = 135\,\mu m$ resulting in a magnification $\simeq 2.3$, that leads to a total magnification $M_{tot} = M_T\, M_{obj} \simeq 2.3 \times 20 \simeq 46$. When the microlenses are coupled to a 25X water immersion objective, the images of the cells through the microlenses can be recovered at $\delta z = 43\,\mu m$, corresponding to a microlens magnification $M_T \simeq 1.75$, that leads to a total magnification $M_{tot} = M_T\, M_{obj} \simeq 1.75 \times 25 \simeq 44$. Indeed the raster scanning images obtained with the two microscope objectives are quite similar. The field of view (FOV) is reduced by a three/fourfold factor, with respect to the FOV of the objectives, depending on the coupling distance between the microlenses and the objective.

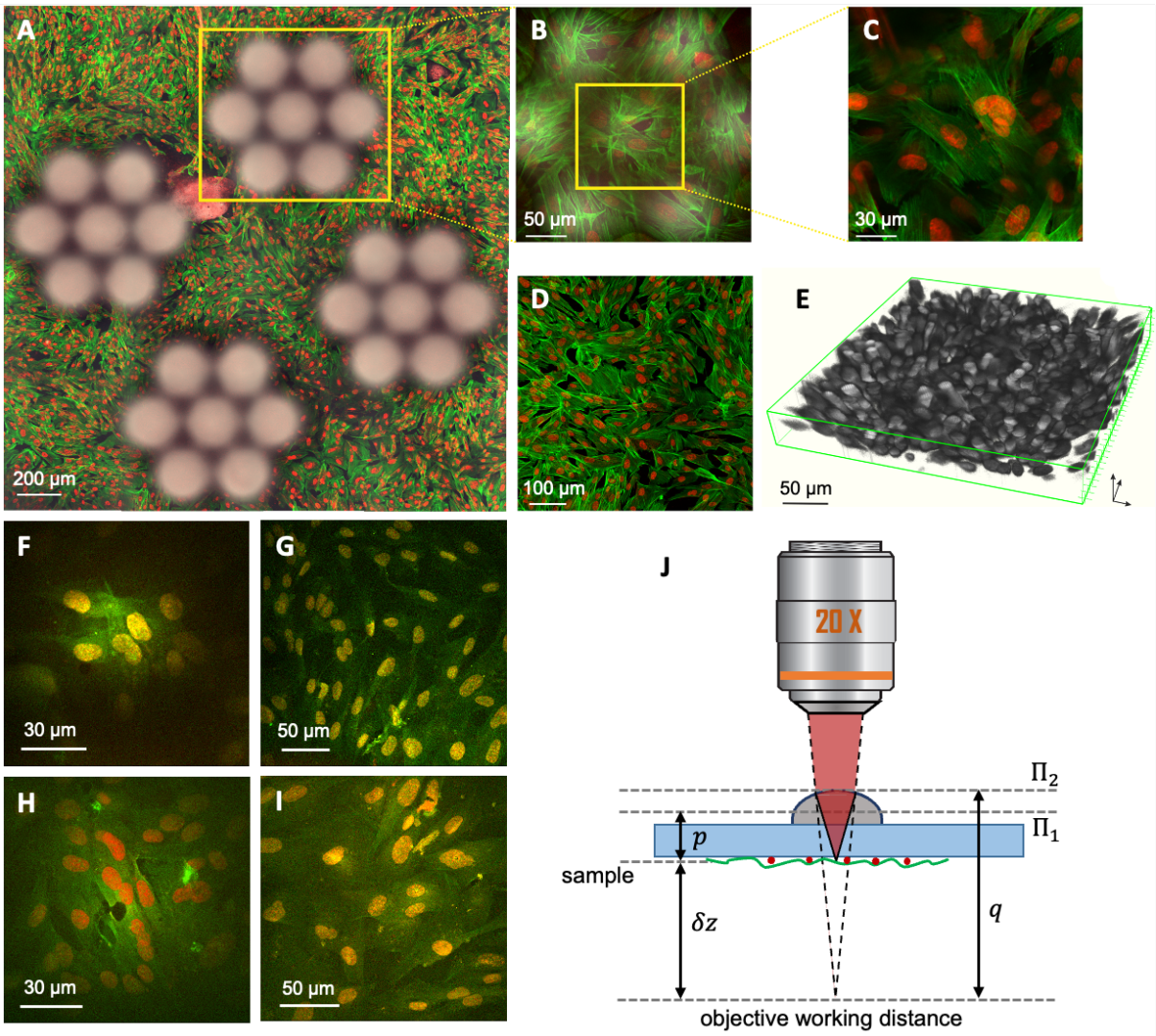

Figure 6. A: Confocal image (3x3 stitched tiles) of stained human fibroblasts (FITC-phallodin and DRAQ5 staining). The fluorescence confocal and transmitted images at the glass coverslip focal plane are superimposed. Microlenses are imaged through out-of-focus transmitted laser light. Cell nuclei, in red, and cytoskeleton, in green, are visualized in fluorescence (actin, excitation at 488 nm, emission at 525/50 nm; nuclei, excitation at 647 nm, emission at 665/81 nm). **B**: Full field-of-view fluorescence confocal image through an array of microlenses, superimposed to the transmitted-light image. The cell fluorescence image is collected when the sample is shifted by $\delta z = 165\ \mu m$ with respect to the objective focal plane. **C**: Cropped scan area through a single microlens. **D**: Full field-of-view confocal microscope image of cells at the glass coverslip focal plane ($\delta z \simeq 0$, scale bar $100 \mu m$). A 20x dry objective was employed for **A-D**. **E**: 3D reconstruction of cells through an array of microlenses. The image was rescaled accordingly to the microlenses magnification: $M_T \simeq 2.4, M_z \simeq {M_T}^2$. **F-I:** Fluorescence images of the cells under two-photon excitation ($\lambda = 800 nm$). **F**: Fluorescence image collected through the microlenses coupled to a 20x dry objective at a distance $\delta z = 135\ \mu m$ (with respect to the objective sample plane), resulting in a total magnification $M_{tot} \simeq 45$. **G**: Control image obtained through the 20x dry objective at $\delta z \simeq 0$. **H**: Image of the cells through the microlenses coupled to a 25x water immersion objective obtained at $\delta z \simeq 43\ \mu m$. **I:** Control image obtained with the 25x water immersion objective when $\delta z \simeq 0$. **J**: Sketch of the configuration used to couple the microlens with the optical scanning microscope. The

distance between the sample (dark gray) and its virtual image (light gray) through the microlens is δz. Π_1 and Π_2 are the two principal planes of the microlens.

Conclusions.

In summary, we have shown that microlenses can be fabricated with a medium throughput, about 8 minutes/lens, by limiting the 2PP fabrication to a $\simeq 1\ \mu m$ thick outer crust and a post-development volume polymerization. This procedure leads to a 98% reduction in the fabrication time with respect to volume polymerization, still obtaining sufficient optical quality to use the lenses for direct widefield imaging of cells, both in transmission and in fluorescence mode. No evidence of inhomogeneities in the lens volume is found due to the post-development processing.

Widefield imaging through the microlenses can be obtained in a finite conjugate coupling approach, where the microscope objective and the microlenses are arranged in series. This method can be used for routine testing of the optical quality of the microlenses. More interesting, the microlenses can be coupled to a raster scanning non-linear excitation optical microscope, even by using low numerical aperture and low magnification objectives: in this case a virtual image configuration is adopted. Our experiments (**Fig.6**) show for the first time that it is possible to use the microfabricated lenses to efficiently induce non-linear excitation and collect two-photon excitation images from cells with the same level of laser intensity and similar signal to noise ratio. This work opens the possibility to implement micro-optical devices for non-linear excitation that, due to the limited size, could be used as implants for the direct and continuous optical inspection of biological dynamics *in vivo*.

MATERIALS and METHODS

Sample Preparation for Two-Photon Laser Polymerization:

The photoresist used for the 2PP of the microlenses was a negative hybrid organic-inorganic UV-curable resist known as SZ2080TM,[34] biocompatible and validated for biological applications.[6,35] To increase the efficiency of the polymerization 1% of Irgacure-369 (2-Benzyl-2-dimethylamino-1-(4-morpholinophenyl)-butanone-1) is added to the resist as photoinitiator. About 46 µl of liquid SZ2080 photoresist were deposited by drop casting on a

12 mm diameter circular glass coverslip with a thickness between 170 and 230 μm (#1.5, Menzel-Glaser, Germany). To allow the drying of the resist thus to prevent any unwanted sliding of the structures during the fabrication process, the samples were left under the chemical hood for 48 hours. Once the material had condensed, the photoresist reached a semi-solid state suitable for the further laser-induced polymerization.

Two-Photon Laser Polymerization Setup:

The 2PP fabrication was performed by a femtosecond Ytterbium (Yb) fiber laser (Satsuma, Amplitude System). The laser wavelength was 1030 nm, the pulse duration is ~280 fs and the repetition rate was fixed to 1MHz. The output power reaches a maximum value of 10 W. The laser beam passed through a series of mirrors that steered it to a 2x telescope and a half-wave plate coupled to a polarizer (MPS50GR-TTM-G80-DC-LMO-PLOTS, Aerotech, USA) which was used as a system for the power control. The half-wave plate was mounted on a software controlled motorized rotator which allows the dynamic control of the power during 2PP. At the end of the optical path the beam was tightly focused by a water matched CFI plan 100XC W objective with a numerical aperture (NA) 1.1 (Nikon, Japan) directly onto the photosensitive resist. The sample was mounted within a glass container with a diameter of 100 mm connected to a gimbal mechanical system (Gimbal Mounts 100, Thorlabs). The sample holder-gimbal complex was screwed on a planar (X, Y) translational stage (ANT95-50-XY, Aerotech, USA) while the motion of the objective along the Z-direction was controlled by a high resolution linear stage (ANT130-035-L-ZS, Aerotech, USA) balanced by two air compressed pneumatic pistons. The motion of this three-axes stages was controlled by software (Automation 3200 CNC Operator Interface, Aerotech, USA) as well as the half-wave plate rotation and they were provided with a feedback position and velocity control system with a resolution on the order of 200 nm. For a real time monitoring of the writing process within the working area, as well as the polymerization process, a red-light emitting diode illumination was positioned in the empty central cavity of the gimbal, under the sample holder-gimbal complex, and a CCD camera was mounted behind a dichroic mirror (Thorlabs, Germany). The three translational stages and all the components of the optical path were placed upon a granite table (Zali Precision Granite Technology, Italy).

The outer surface of each microlens was two-photon polymerized directly focusing the laser beam into the SZ2080 photoresist droplet, moving the sample at a speed of 1 mm/s. Due to laser radiation absorption, the pulse energy used for 2PP of the microlenses depends on the SZ2080 droplet thickness thus ranging from 13 nJ to 15 nJ (at the objective entrance pupil).

Sample Development and UV Exposure:

After the two-photon polymerization process, the samples underwent a development procedure to remove the unpolymerized photoresist surrounding the volume of the microfabricated microlenses. The samples were soaked in a glass beaker filled with a 50% v/v 2-pentanone, 50% v/v isopropyl alcohol solution (Sigma-Aldrich, USA). After 30 min, they were cautiously washed with a few drops of isopropyl alcohol then gently dried by room temperature Nitrogen. Afterwards, the sample was UV irradiated passing through the glass substrate in order to avoid the direct and additional exposure of the previously polymerized surface. Consequently thus the radiation intensity and the time of exposure depend on the thickness of the substrate, the volume of photoresist to be polymerized and the shape of the lens. Therefore, the process was optimized exposing the sample to 300 mW of UV irradiation (λ=385nm) for 120 seconds (LIGHTNINGCURE LC-L1V3) in order to crosslink the

unpolymerized core of the lens achieving the structural stability without causing resin degradation.

Optical and Scanning Electron Microscopy Qualitative Characterization:
Qualitative analysis of fabrication outcomes in terms of shape and mechanical stability were performed by an optical microscope with different magnitudes 4×, 10×, 20×, 40× (Eclipse ME600, Nikon, Japan) and by a scanning electron microscope (SEM, Phenom Pro, Phenom World, Netherlands). The SEM observations were carried out at 10 kV.

Profilometry Analysis:
The analysis of the overall shape of the lenses were performed by a surface profilometer (KLA Tencor P-17) using a 2.5 um stylus tip radius and setting the scan speed as 20 μm/s, 20 Hz sampling rate, 1 mg as the down force to be applied on the sample surface (see **SI6**, **"Profilometer analysis of the shape of the microlenses"**, and **Fig.SI6**). The scanning of each lens was performed by sampling it each 5 μm along both the planar directions (X,Y) and both the positive and negative sense, within a scanning box of 350 μm side. Lastly, the surface profile has been interpolated with a spheric function in order to evaluate the reliability of the fabrication with respect to the lens model.

Fluorescence Microscopy:
For confocal imaging human dermal RFP fibroblasts (Innoprot, Spain) were cultured in Dulbecco's modified Eagle's medium (DMEM) supplemented with 10% fetal bovine serum, 1% L-glutamine (2 mM), penicillin (10 units/ml),and streptomycin (10 μg/ml) at 37°C and 5% CO_2. Then, 20k/50μl cells were drop-seeded on borosilicate glass coverslips,and after 4 hours of incubation, diluted in 3 ml of DMEM and expanded for 48 hours. Then, cell culture was fixed in 4% paraformaldehyde (Sigma Aldrich, Italy) for 5 minutes and stained, for nuclei identification, with: DRAQ5 (ThermoFisher Scientific, Italy) in a dilution ratio of 1:1000 in PBS for 15 minutes and with 1 μg/ml Hoechst 33342 (ThermoFisher Scientific, Italy) for 10 minutes at room temperature. Finally, cells were incubated for 45 minutes with 1 μg/ml of FITC-phalloidin (Sigma Aldrich, Italy), to stain actin cytoskeleton. The images were taken on a A1R+ Nikon (Nikon, Japan) confocal microscope equipped with an apochromat, 20X, NA 0.8 dry objective lens. Images were taken by exciting at $\lambda = 488$ nm for actin filaments stained with FITC (emission collected through a 525/50 nm band pass filter) and at $\lambda = 561$ nm for nuclei stained with DRAQ5 (emission collected through a 665/81 nm band pass filter).
Wide-field fluorescence images were taken on a Leica SP5 microscope equipped with a 20X dry objective (HC PL Fluotar, NA=0.5).

Two-photon Excitation Fluorescence Microscopy:
Two photon fluorescence microscopy was performed on a custom setup based on a BX51 (Olympus, Japan) direct microscope equipped with either a water immersion long working distance objective (XL Plan N, 25X, NA=1.05, Olympus, Japan) or a dry objective (Plan N, 20X, NA=0.4, Olympus, Japan). The raster scanning images were acquired through a M610 (ISS Inc., Urbana-Champaign, USA) scanning head coupled to a Ti:Sapph laser (MaiTai DeepSee, Newport, USA) and to two analog photomultiplier tubes (HC125-02, Hamamatsu, Japan).

Optical Characterization of Microlenses:

In all the optical characterization the source was a fiber coupled 635 nm laser diode (HLS635 + P1-630A-FC-1 single mode fiber) collimated by a plan 4X, NA=0.10 objective (Olympus, Japan).

Wavefront Measurements:
The wavefront was measured by means of a Shack-Hartman sensor (WFS20-K1/M, Thorlabs, USA) with a 150 µm pitch array of lenses. A planar Gaussian beam overfills the microlens pupil to be tested. Part of the beam is focused by the microlens on the focal plane of a 63X dry objective that collimates it at its exit pupil (**Fig.SI4.1**). A 4f telescope conjugates the electromagnetic field from the objective exit pupil plane, magnifying it on the entrance pupil of the Shack-Hartman sensor. The fraction of the light that is not captured by the microlens is filtered at the intermediate plane of the 4f telescope by a pinhole (**Fig.SI4.1**), to single out only the wavefront of the beam focused by the microlens.

Beam profile test:
The minimum spot size that can be obtained through the microlenses was measured on an infinity conjugated microscope. The tube lens and the camera sensor (UI-1542LE-M, IDS, Obersulm, D) were carefully aligned to accept rays from infinity, so that the microscope objective collects the electromagnetic field in its front focal plane. The images collected by the camera at various positions of the focal plane of the objective give us the shape of the intensity profile generated by the microlenses.

Acknowledgments.
Part of the experimental characterization was performed at PoliFAB, the micro and nanofabrication facility of Politecnico di Milano (www.polifab.polimi.it). The authors would like to thank the PoliFAB staff for the valuable technical support.
This research has received funding from the European Union under the Horizon 2020 research and innovation program (G.A. No. 964481 – IN2SIGHT).

BIBLIOGRAPHY.

[1] F. Mingozzi, R. Spreafico, T. Gorletta, C. Cigni, M. Di Gioia, M. Caccia, L. Sironi, M. Collini, M. Soncini, M. Rusconi, U. H. von Andrian, G. Chirico, I. Zanoni, F. Granucci, *EMBO Mol. Med.* **2016**, *8*, 1039.
[2] D. U. Pizzagalli, A. Pulfer, M. Thelen, R. Krause, S. F. Gonzalez, *Front. Immunol.* **2022**, *12*.
[3] E. Dondossola, B. M. Holzapfel, S. Alexander, S. Filippini, D. W. Hutmacher, P. Friedl, *Nat. Biomed. Eng.* **2017**, *1,7*, 1.
[4] E. Dondossola, P. Friedl, *Nat. Rev. Mater.* **2022**, *7*, 6.
[5] C. Prunier, N. Chen, L. Ritsma, N. Vrisekoop, *Methods* **2017**, *128*, 52.
[6] C. Conci, E. Jacchetti, L. Sironi, L. Gentili, G. Cerullo, R. Osellame, G. Chirico, M. T. Raimondi, *Adv. Opt. Mater.* **2022**, *2101103*, 1.
[7] V. Ntziachristos, *Nat. Methods* **2010**, *7*, 603.
[8] A. A. Gopal, A. Kazarine, J. M. Dubach, P. W. Wiseman, *Int. J. Biochem. Cell Biol.* **2021**, *130*.
[9] F. P. Bolin, L. E. Preuss, R. C. Taylor, R. J. Ference, *Appl. Opt.* **1989**, *28*, 2297.
[10] C. N. LaFratta, J. T. Fourkas, T. Baldacchini, R. A. Farrer, *Angew. Chemie Int. Ed.* **2007**, *46*, 6238.
[11] M. Bouzin, A. Zeynali, M. Marini, L. Sironi, R. Scodellaro, L. D'alfonso, M. Collini, G.

Chirico, *Multiphoton laser fabrication of hybrid photo-activable biomaterials*, Vol. 21, MDPI, **2021**, pp. 1–36.

[12] A. Zeynali, M. Marini, G. Chirico, M. Bouzin, M. Borzenkov, L. Sironi, L. D'Alfonso, P. Pallavicini, V. Cassina, F. Mantegazza, F. Granucci, L. Marongiu, D. Polli, A. De la Cadena, M. Collini, *Adv. Opt. Mater.* **2020**, *8*, *2000584*, 1.

[13] M. Marini, A. Zeynali, M. Collini, M. Bouzin, L. Sironi, L. D'Alfonso, F. Mantegazza, V. Cassina, G. Chirico, *Lab Chip* **2022**.

[14] R. Guo, S. Xiao, X. Zhai, J. Li, A. Xia, W. Huang, *Opt. Express* **2006**, *14*, 810.

[15] J. Li, P. Fejes, D. Lorenser, B. C. Quirk, P. B. Noble, R. W. Kirk, A. Orth, F. M. Wood, B. C. Gibson, D. D. Sampson, R. A. McLaughlin, *Sci. Rep.* **2018**, *8*, 1.

[16] T. Gissibl, S. Thiele, A. Herkommer, H. Giessen, *Nat. Photonics* **2016**, *10*, 554.

[17] T. Gissibl, S. Thiele, A. Herkommer, H. Giessen, *Nat. Commun.* **2016**, *7*.

[18] M. F. Griffin, H. E. desJardins-Park, S. Mascharak, M. R. Borrelli, M. T. Longaker, *Dis. Model. Mech.* **2020**, *13*, 1.

[19] M. A. May, N. Barré, K. K. Kummer, M. Kress, M. Ritsch-Marte, A. Jesacher, *Nat. Commun.* **2021**, *12*.

[20] I. N. Papadopoulos, J. S. Jouhanneau, J. F. A. Poulet, B. Judkewitz, *Nat. Photonics* **2017**, *11*, 116.

[21] V. Lakshminarayanan, A. Fleck, *J. Mod. Opt.* **2011**, *58*, 545.

[22] M. V. Klein, T. E. Furtak, *Optics*, 2nd ed., J. Wiley &Sons, New York, **1991**.

[23] A. Žukauskas, G. Batavičiute, M. Ščiuka, Z. Balevičius, A. Melninkaitis, M. Malinauskas, *Opt. Mater. (Amst).* **2015**, *39*, 224.

[24] D. Wu, S.-Z. Wu, L.-G. Niu, Q.-D. Chen, R. Wang, J.-F. Song, H.-H. Fang, H.-B. Sun, *Appl. Phys. Lett.* **2010**, *97*, 031109.

[25] M. Malinauskas, H. Gilbergs, A. Žukauskas, V. Purlys, D. Paipulas, R. Gadonas, *J. Opt.* **2010**, *12*, 035204.

[26] M. Malinauskas, A. Žukauskas, V. Purlys, K. Belazaras, A. Momot, D. Paipulas, R. Gadonas, A. Piskarskas, H. Gilbergs, A. Gaidukevičiūtė, I. Sakellari, M. Farsari, S. Juodkazis, *J. Opt.* **2010**, *12*, 124010.

[27] T.-T. Chung, Y.-T. Tu, Y.-H. Hsueh, S.-Y. Chen, *Int. J. Autom. Smart Technol.* **2013**, *3*, 131.

[28] J.-G. Hua, H. Ren, A. Jia, Z.-N. Tian, L. Wang, S. Juodkazis, Q.-D. Chen, H.-B. Sun, *Opt. Lett.* **2020**, *45*, 636.

[29] D. Gonzalez-Hernandez, S. Varapnickas, G. Merkininkaitė, A. Čiburys, D. Gailevičius, S. Šakirzanovas, S. Juodkazis, M. Malinauskas, *Photonics* **2021**, *8*, 577.

[30] Y. Hu, Y. Chen, J. Ma, J. Li, W. Huang, J. Chu, *Appl. Phys. Lett.* **2013**, *103*, 141112.

[31] M. Born, E. Wolf, *Principles of Optics*, Pergamon Press, **1959**.

[32] M. Bouzin, G. Chirico, L. D'Alfonso, L. Sironi, G. Soavi, G. Cerullo, B. Campanini, M. Collini, *J. Phys. Chem. B* **2013**, *117*, 16405.

[33] X. Zhang, T. Kashti, D. Kella, T. Frank, D. Shaked, R. Ulichney, M. Fischer, J. P. Allebach, In *Image Quality and System Performance IX*, SPIE, **2012**, p. 829307.

[34] A. Ovsianikov, J. Viertl, B. Chichkov, M. Oubaha, B. MacCraith, I. Sakellari, A. Giakoumaki, D. Gray, M. Vamvakaki, M. Farsari, C. Fotakis, *ACS Nano* **2008**, *2*, 2257.

[35] M. T. Raimondi, S. M. Eaton, M. Laganà, V. Aprile, M. M. Nava, G. Cerullo, R. Osellame, *Acta Biomater.* **2013**, *9*, 4579.

Microlenses fabricated by two-photon laser polymerization for intravital cell imaging with non-linear excitation microscopy

SUPPLEMENTARY MATERIALS

M. Marini[1,+], A. Nardini[3,+] , R. Martínez Vázquez[2,+], C. Conci[3], M. Bouzin[1], M. Collini[1], R. Osellame[2], G. Cerullo[4], B.S. Kariman[4], M. Farsari[5], E. Kabouraki[5], M.T. Raimondi[3,+,*] , G. Chirico[1,+,*].

1 Department of Physics, Università degli Studi di Milano-Bicocca, Piazza della Scienza 3, 20126, Milan, Italy
2 Institute for Photonics and Nanotechnologies (IFN), CNR, Piazza L. da Vinci 32, 20133 Milan, Italy
3 Department of Chemistry, Materials and Chemical Engineering "Giulio Natta", Politecnico di Milano, Piazza L. da Vinci 32, 20133 Milan, Italy
4 Department of Physics, Politecnico di Milano, Piazza L. da Vinci 32, 20133 Milan, Italy
5 FORTH/IESL, N. Plastira 100, 70013, Heraklion, Greece

+: contributed equally to the work
*: corresponding authors.

Table of content

1. **Refraction index of tissues.**
2. **Effect of the inhomogeneity of the propagating medium on the spherical aberrations.**
3. **Microlenses coupled to a raster scanning optical microscope.**
4. **Microlens wavefront measurement.**
5. **Field of view of microlenses.**
6. **Profilometer analysis of the shape of the microlenses.**
7. **Intensity distribution sampling along the optical axis.**

SI1. Refraction index of tissues.

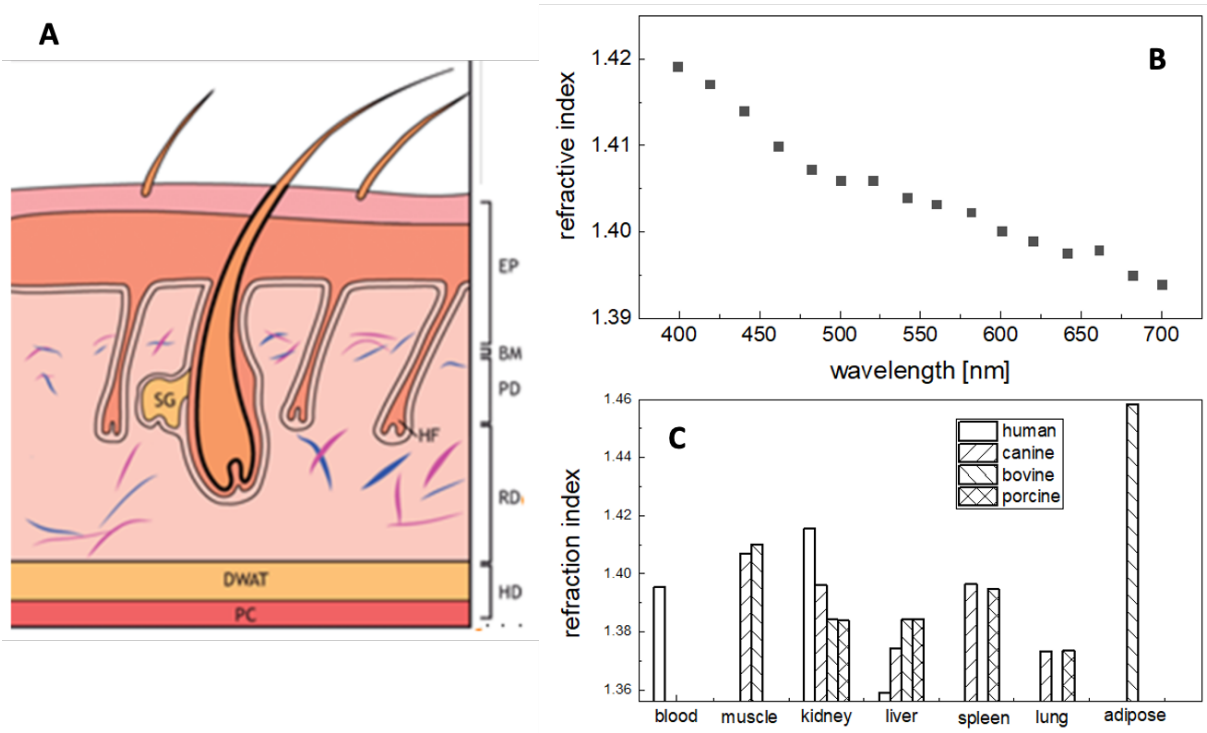

Figure SI1. A: The structure of mouse skin. EP: epidermis; BM: basement membrane; PD, papillary dermis; RD, reticular dermis; HD: hypodermis; DWAT: dermal white adipose tissue; PC: panniculus carnosus; HF: hair follicle;SG: sebaceous gland; . Adapted (CC common) from ref. [1]. The skin has a high density of fibroblasts (blue and purple). **B**: Trend of the refractive index of a sample of mouse muscle as a function of the wavelength (open squares), together with the best fits to a linear trend (solid blue line, $y = 1.45 - 7.74 \times 10^{-5}\ \lambda$) and to a power law (solid red line, $y = 1.37 + 180.44\,\lambda^{-1.4}$) (fit on the data taken from ref.[2]). **C**: Refractive index values for various tissues and animals at $\lambda = 633\ nm$ as from ref. [2].

SI2. Effect of the inhomogeneity of the propagating medium on the spherical aberrations.

In order to evaluate the effect of the inhomogeneity of the propagating medium on the possibility to tightly focus a collimated laser beam, we have studied an aspheric lens 25 mm in diameter with an effective focal length in air of about 25 mm.
The lens sag surface is given by:

$$z(r) = C * r^2 /(1 + \sqrt{1 - C^2 r^2}) \; + \; A_2 r^2 \; + A_4 r^4 \; + A_6 r^6$$
$$C = 1/12.6\, mm^{-1}\,;\; A_2 \; = 3.34 \times 10^{-3} \; mm^{-2};$$
$$A_4 \; = -2.06 \times 10^{-5} \; mm^{-4};\; A_6 \; = \; 5.87 \times 10^{-8}\, mm^{-6}; A_8 \; = -2.80 \times 10^{-9}\, mm^{-8}$$

The lens is aspherical for propagation in water (n_1 =1.34 at $\lambda = 0.8\, \mu m$) for a pupil size of 15 mm. We have then simulated the propagation of light through an inhomogeneous medium composed of a first layer (thickness d_1) of water and a second layer (thickness $d_2 = f - d_1$, where f is the lens focal length) of a medium with $n_2 \; = \; 1.45$ (**Fig.SI2.1A**). The propagation was computed for a wavelength $\lambda = \; 0.8\, \mu m$ for a beam coaxial with the optical axis. The phase profiles at the focal plane (minimum confusion circle) for the propagation in pure water and in the inhomogeneous medium ($d_1 = 10\, mm$), for a pupil size of 22 mm, are reported in **Fig.SI2.1B** and **Fig.SI2.1C**, respectively. The aberrations are primarily spherical aberrations and can be described by the Zernike Polynomial with coefficient $a_{4,0}$. The spherical aberration rises rapidly with the pupil size, as expected[3], and almost doubles its value at 80% of the pupil size when moving from a homogeneous medium to an inhomogeneous medium (see **Fig.1B,** main text). The increase of the spherical aberration coefficient $a_{4,0}$ depends almost linearly on the refraction index changes between the medium layers (**Fig.1B,** main text).
Regarding the minimum spot size of a laser beam in the homogeneous and inhomogeneous cases, we can measure it from the simulated physical propagation of a Gaussian beam 9 mm in waist on the lens. We notice that circular fringes arising from spherical aberrations are evident in the inhomogeneous case (**Fig.SI2.1E**) and prevent a clear measurement of the minimum spot size (beam waist at $1/e^2$ of the maximum intensity). By force fitting the intensity distribution to a Gaussian beam, we can however estimate beam sizes of the order of $5\, \mu m$ and $25\, \mu m$ for the two cases, respectively. This would imply a huge variation of the excitation probability under two-photon regime.

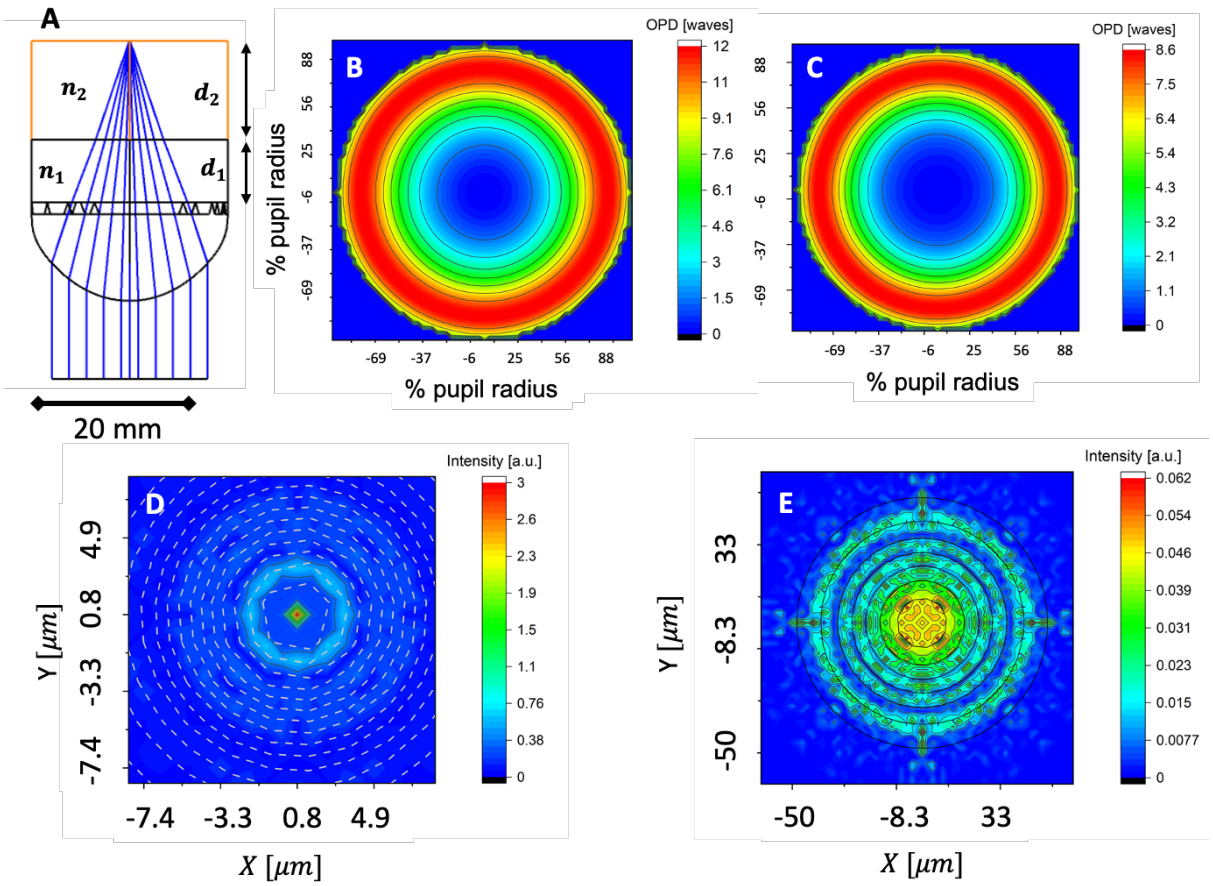

Figure SI2.1. Spherical aberrations in inhomogeneous media. **A**: Simulated propagation of a parallel beam focused by a 25-mm focal length, 25-mm diameter, plano-aspherical lens through an inhomogeneous medium composed of a first layer (thickness d_1) of water and a second layer (thickness d_2) of a medium with $n_2 = 1.50$. **B:** Optical path difference (OPD) profiles at the focal plane (minimum confusion circle) for the propagation in the inhomogeneous medium (**B**, $d_1 = 10\ mm$) and in pure water (**C**) for a pupil size of 22 mm. **D-E**: Beam intensity distribution at the focal plane for the homogeneous (**D**) and inhomogeneous ($d_1 = 8\ mm$, **E**) medium. The pupil size was 20 mm.

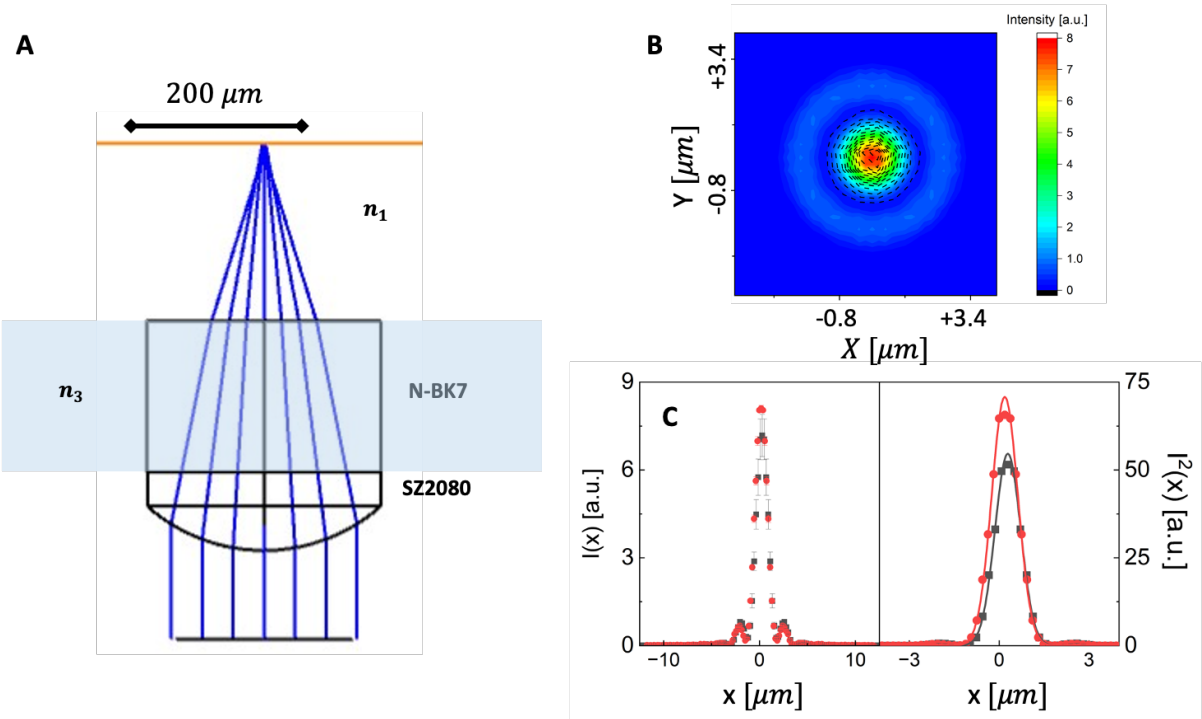

Figure SI2.2. Simulation of the beam profile at the focal plane of the microlens (see table I in the main text for the geometrical parameters). **A**: Sketch of the microlens fabricated on a borosilicate glass slide. **B**: Beam intensity distribution at the focal plane of the microlens. **C:** Left plot: profile of the radial intensity of panel B for the case of propagation in air (red symbols) and in water (black symbols). Right plot: profile of the radial dependence of the square of the intensity at the focal plane (panel B) for the case of propagation in air (red symbols) and in water (black symbols) together with the best fit Gaussian distribution (solid lines) whose beam waists are $1.20 \pm 0.03\,\mu m$ and $1.23 \pm 0.03\,\mu m$ for the propagation in air and water, respectively.

SI3. Microlenses coupled to a raster scanning optical microscope.

The microlenses can be coupled to an optical microscope in two ways: a finite conjugate setup (**Fig.SI3.1A**) and a virtual image setup (**Fig.SI3.1B**). In both cases we assume to use infinity corrected objectives.

In the first case, the microlens creates a real image of a sample in the focal plane of the objective (**Fig.SI3.1A**). The distances of the sample (p) and of the image (q) planes must be measured with respect to the principal planes and are related to the focal length of the microlens f_μ by $q = p(1 - f_\mu)/f_\mu$. The principal planes are at the vertex of the spherical surface and at a fraction of the total thickness (D) of the lens equal to $D/n_L \simeq 258\ \mu m/1.49 \simeq 173\ \mu m$. The thickness is evaluated by summing the thickness of the lens itself and of the borosilicate glass slide and we take an average of the refractive index of the SZ2080 resist ($n_{SZ2080} \simeq 1.46$) and that of borosilicate ($n_{BK7} \simeq 1.52$). The second principal plane lies therefore approximately on the edge between the lens and the glass slide (**Fig. SI3.1A**).

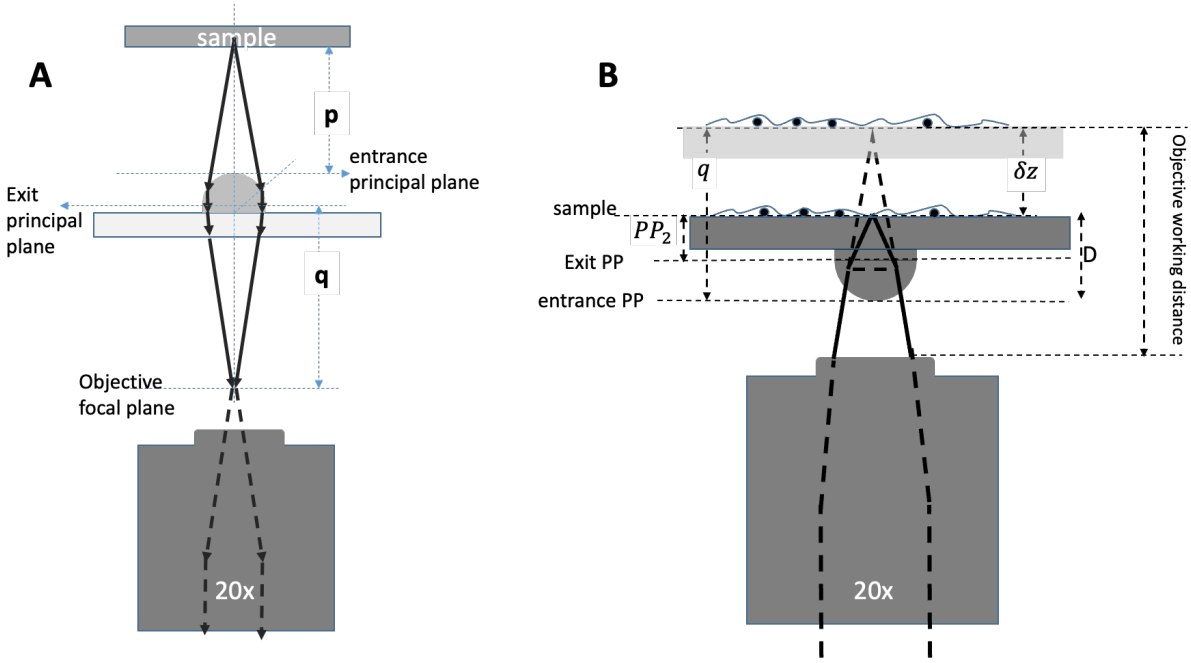

Figure SI3.1. Schematic representation of the two possible coupling modes of the microlens with a microscope objective lens. **A**: Finite conjugate coupling between the micro-lens and an objective lens. **B**: The microlens is set at a distance from the exit lens of the microscope objective that is smaller than the objective lens working distance. In this case the microlens creates a virtual image collected by the objective lens. The grayish replica of the sample in the sketch represents the position of the sample for conventional imaging with no microlens in the optical path.

In a second approach the objective lens collects the virtual image of the sample created by the microlens (**Fig.SI3.1B**). In the embodiment realized for this work, the sample (a cell culture) lies on the same glass slide where the microlenses are fabricated. Since the cell

culture is approximately bidimensional, the distance p of the sample to the corresponding principal plane is approximately the position, PP_2, of the principal plane with respect to the surface of the coverglass. The distance q of the image plane to the corresponding principal plane corresponds to the full thickness of the microlens device (D in **Fig.SI3.1B**) plus the displacement δz by which we need to move the microscope objective to get an image through the microlens. The magnification of the resulting image corresponds to $M = M_T M_{obj}$, where M_{obj} is the objective magnification and $M_T = q/p = (D + \delta z)/PP_2$ is the transverse magnification of the microlens ($PP_2 \simeq 173\ \mu m$).

A simulation of the raster scanning through the microlens compared to the raster scanning without the microlens is reported in **Fig.SI3.2**.

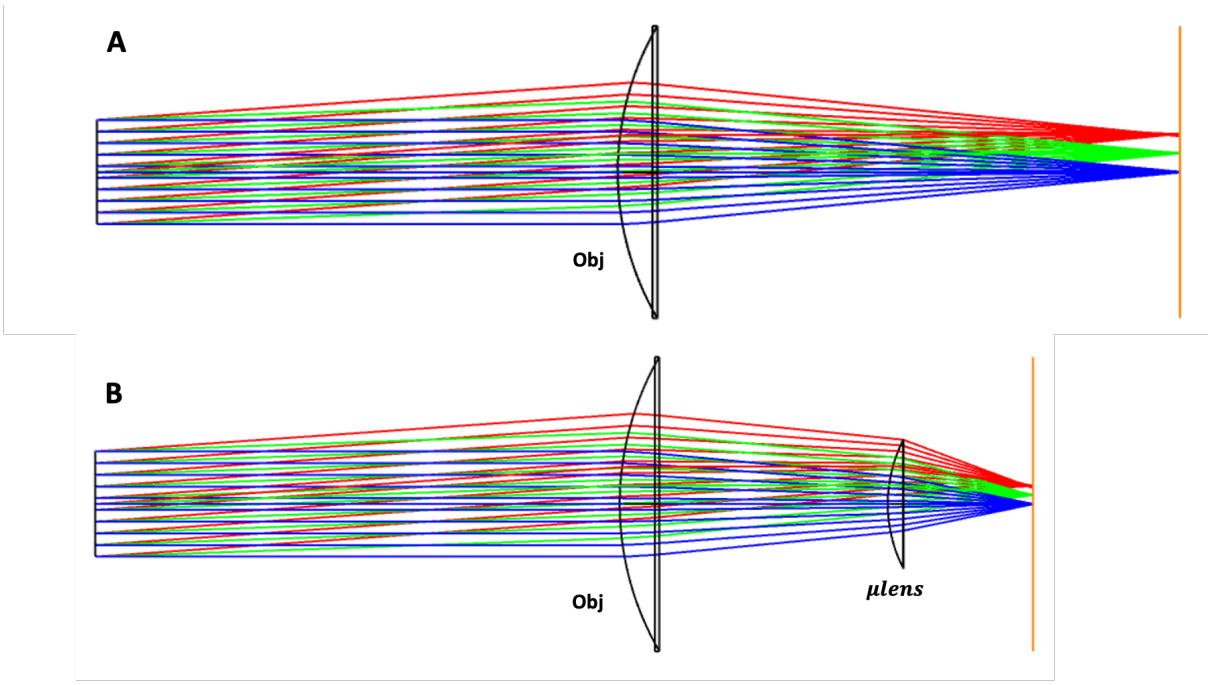

Figure SI3.2 Raster scanning through a microlens. **A**: Simulation of the raster scanning of a conventional scanning microscope, where the objective lens has been approximated with a single telecentric lens. **B**: Same raster scanning of panel A when a microlens is placed between the objective plane and the sample plane. Note that the microlens increases the overall numerical aperture of the system and consequently reduces the field of view by a factor M_T (calculated above and corresponding to the magnification of the microlens).

SI4. Microlens wavefront measurement.

The wavefront was measured by means of a Shack-Hartman sensor (WFS20-K1/M, Thorlabs, USA) with a 150 μm pitch array of lenses. The optical configuration adopted (**Fig.SI4.1**) allows us to test the lenses by focusing a collimated beam. A planar Gaussian beam impinges on the microlens to be tested with a $1/e^2$ size of about 9 mm. Part of the beam is focused by the microlens on the focal plane of a 63X dry objective (Zeiss A-Plan 63x, NA= 0.8). The electromagnetic field is sampled by the 63X objective lens and collimated at its exit pupil. A 4f telescope conjugates the electromagnetic field from the objective exit pupil plane, magnifying it on the entrance pupil of the Shack-Hartman sensor. The fraction of the light that is not captured by the microlens is filtered at the intermediate plane of the 4f telescope by a pinhole (PH in **Fig.SI4.1**). In this way it is possible to single out only the wavefront of the beam focused by the microlens.

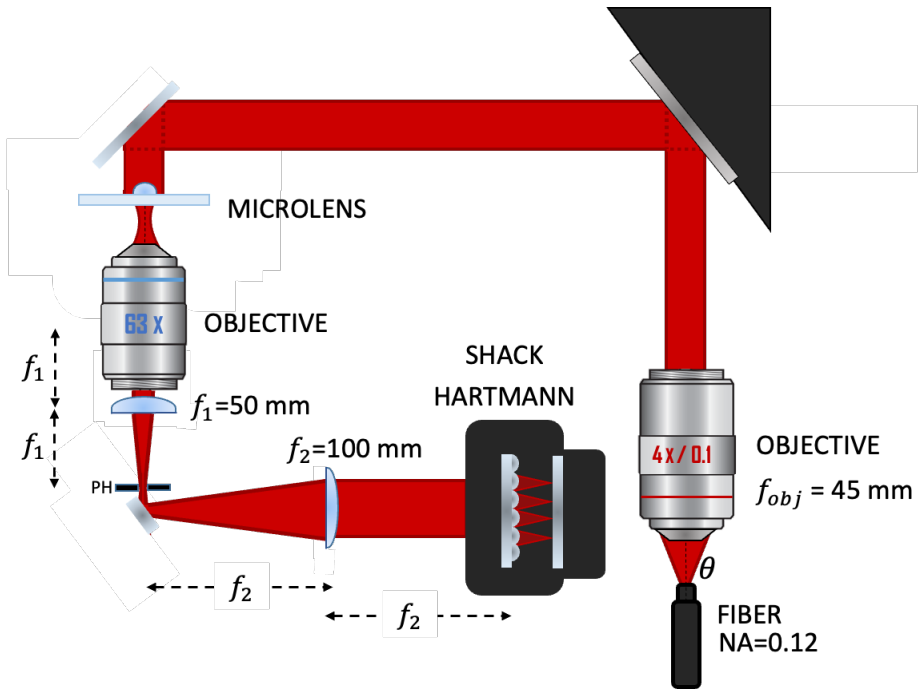

Figure SI4.1. Sketch of the optical setup adopted for the wavefront measurement.

<u>Comparison to theoretical treatments</u>. The microlenses were always tested in the configuration shown in **Fig.SI4.1**, this condition providing minimal spherical aberration[3] and corresponding

to a shape factor $Q = (R' + R)/(R' - R) = +1$, where R' and R are the curvature radii of the two lens surfaces, and an imaging factor $P = 1 - 2q/f$, where f is the lens focal length (ref.[3], p.243]. The prediction of the spherical aberration *of a thin lens* with the Seidel description of the wavefront[3] is $C_{40} = g(n_L)\, a^4/f^3$, where a is the pupil radius and $g(n_L, P, Q)$ is a correction factor that depends on the refraction index of the lens (for $n_L \simeq 1.46$, P=-1, Q=+1, $g \simeq 0.34$). We notice that this expression is valid for a thin lens and that it is based on a description of the wavefront in terms of powers of the pupil radial coordinate, and not in terms of the Zernike polynomials.

The Shack-Hartman (SH) sensor and Zemax software adopt instead a description of the wavefront in terms of the Zernike polynomials, that are labeled according to the Noll's convection[4] and normalized to their corresponding root mean square (RMS) values. In this way, the contribution of each polynomial to the wavefront RMS is 1 (for the spherical aberration polynomial, ${Z_4}^0$, the RMS value is $\sqrt{5}$). Therefore, the spherical aberration amplitude (i.e. the coefficient of ${Z_4}^0$ in the description of the wavefront) measured by the SH sensor, ${a_{4,0}}^{(SH)}$ should be equal to the one provided by Zemax, ${a_{4,0}}^{(Z)} = {a_{4,0}}^{(SH)}$. If we wanted to compare the amplitude of the spherical aberration predicted by the Seidel description (see ref.[3], Eq. 4.88), ${a_{4,0}}^{(S)}$, to the one given in terms of the Zernike polynomials, ${a_{4,0}}^{(Z)}$, we would need to take into account an additional normalization factor $6/\sqrt{2}$ (see ref. [5] Eq.9 ch. 9.3): ${a_{4,0}}^{(S)} = 6/\sqrt{2}\, {a_{4,0}}^{(SH)}$.

For a *microlens* with the parameters reported in **Table I** (main text), the Seidel prediction is ${a_{4,0}}^{(S)} \simeq 2.8\, \mu m$ that, converted in Noll's notation, is equivalent to an amplitude $\simeq {a_{4,0}}^{(S)}/4.25 \simeq 0.66\, \mu m$. For comparison, the measured value for the microlens is ${a_{4,0}}^{(SH)} = 0.10 \pm 0.01\, \mu m$ (averaged over 3 different microlenses) and the Zemax prediction is ${a_{4,0}}^{(Z)} = 0.15\, \mu m$. This is 50% higher than the measured value, but both values are 4-5 times larger than the Seidel prediction, which is an approximation for a thin lens and it is not sufficient to recapitulate the observations. Indeed, in the experimental evaluation of the aberrations, more than the amplitude of the individual Zernike components describing the wavefront, it is the

wavefront RMS value that can be compared to theoretical predictions. While theoretically the distribution of the Zernike weights is typically well peaked on a specific aberration component (like here on the spherical aberration), experimentally the wavefront is described by a distribution of Zernike polynomials and among them the spherical component, $a_{4,0}$, is the dominant one. As a confirmation of this, we observe that the measured average wavefront RMS is $0.13 \pm 0.02\ \mu m$ that is in good agreement with the Zemax prediction, RMS $= 0.15\ \mu m$. As a comparison to a conventional plano-convex lens, we employed a Thorlabs LA1252 lens with front focal length f=25 mm and 25.4 mm diameter. By using a pupil of about 9 mm size at the entrance of the lens we measured $a_{4,0}{}^{(SH)} \simeq 0.17 \pm 0.02\ \mu m$ and an RMS value $\simeq 0.17\ \mu m$, that compares very well with the RMS value of $0.18\ \mu m$ of the simulated wavefront. However, again, the comparison of the amplitude of the spherical mode computed with the Seidel prediction (see ref.[3], Eq. 4.88] disagrees by a factor of 4 with the measured value, since $a_{4,0}{}^{(S)} \simeq 4.4\ \mu m$ and therefore $6/\sqrt{2}\ a_{4,0}{}^{(SH)} \simeq 0.7\mu m\ \simeq 4a_{4,0}{}^{(SH)}$.

We finally tested the Shack-Hartman setup by measuring the change of the spherical aberration amplitude $a_{4,0}$ as a function of the pupil size for the macroscopic plano-convex lens finding, to a good degree of accuracy, the expected fourth power increase with the pupil size, as demonstrated in **Fig.SI4.2** (solid line).

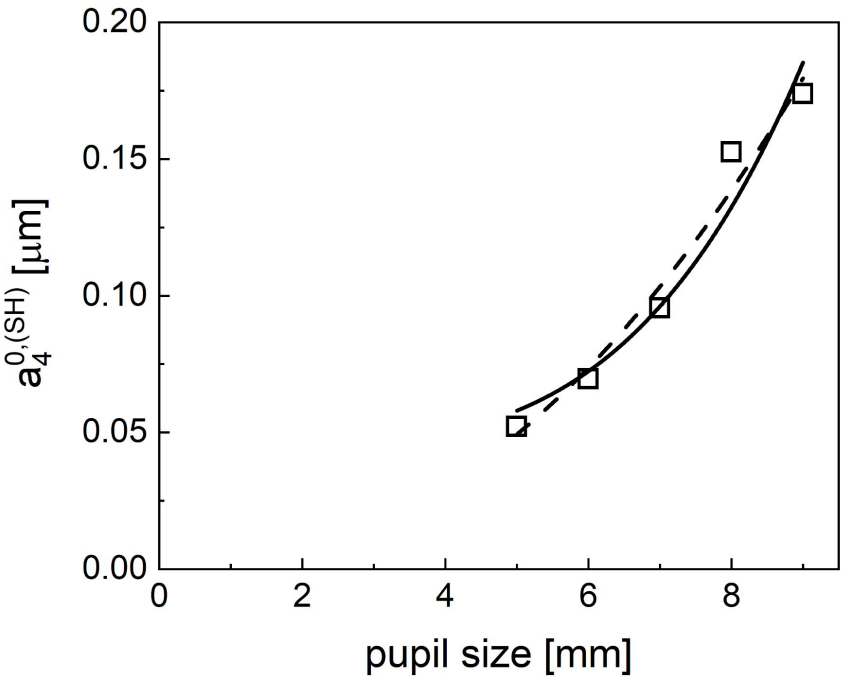

Figure SI4.2 Measurement of the spherical aberration coefficient for a plano-convex lens (Thorlabs, LA1252) as a function of the pupil size. The solid and the dashed lines are the best fits of the trial function $a_{4,0}(p) = A + Bp^m$ to the data with best fit parameters $[A, B, m] = [0.044\ \mu m; 2.1 \times 10^{+6}\ \mu m^{-3}, 4]$ (solid line) and $[A, B, m] = [0\ \mu m; 3.1 \times 10^{+3}\ \mu m^{-1.2}, 2.2]$ (dashed line).

SI5. Field of view of microlenses

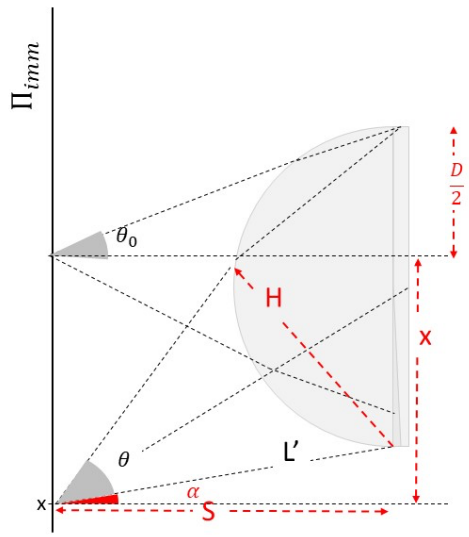

$$\tan(\theta_0) = \frac{D}{2S}$$

$$\tan(\alpha) = \frac{x - \frac{D}{2}}{S}$$

$$\tan(\alpha + \theta) = \frac{x + \frac{D}{2}}{S}$$

$$L' = \sqrt{\left(x - \frac{D}{2}\right)^2 + S^2}$$

$$H = L' sen(\theta)$$

$$P(\theta) = P_0 \left(\frac{D}{H}\right)^2$$

Figure SI5.1 Computation of the field of view of a microlens under wide field imaging. The power collected as a function of the angular position on the sample plane Π_{sample} is computed as $P(\theta) = P_0 (D/H)^2$.

The field of view of a microlens under wide field imaging is computed according to the scheme reported in **Fig. SI5.1**. The power collected as a function of the angular position on the image plane is computed as $P(\theta) = P_0 (D/H)^2$. The field of view is defined as the angular position on the sample plane Π_{sample} where the collected power is 37 % of the maximum collected power on the optical axis. A simulation for different values of the distance S is reported in **Fig.SI5.2**.

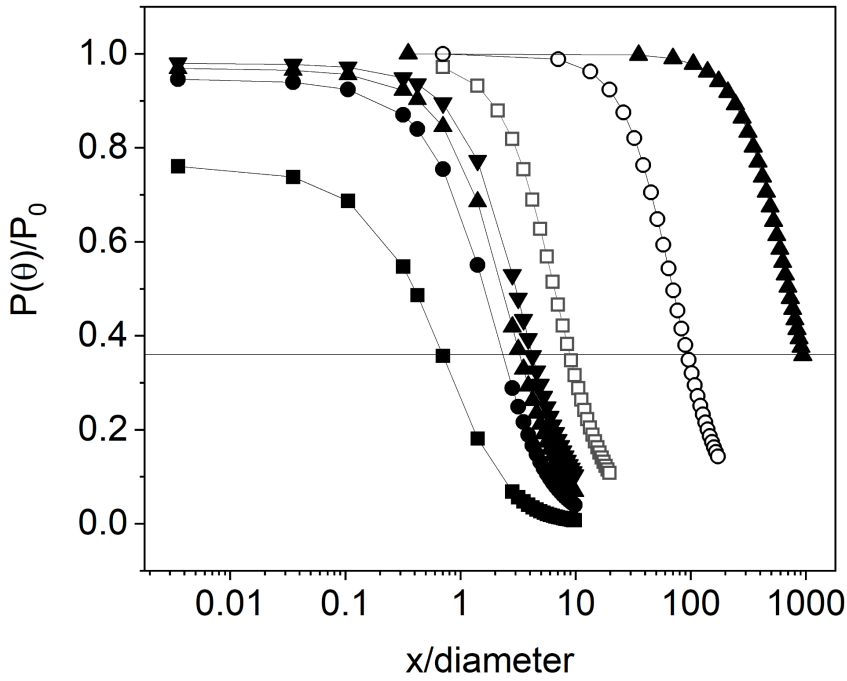

Figure SI5.2. Change of the fraction of the collected power as a function of the angular position on the sample plane for the plano-convex microlens with front focal length $f_{FFL} = 164\ \mu m$. The solid horizontal line indicates the 37% of the maximum power. The symbols correspond to different values of the sample-lens distance S. The lens is approximated as a thin lens for this evaluation: $S = 260 \mu m$ (filled squares), $600\ \mu m$ (filled circles), $800\ \mu m$ (filled up-triangles), $1\ mm$ (filled down-triangles), 2 mm (open squares), 2 cm (open circles), 20 cm (filled up-triangles).

SI6. Profilometer analysis of the shape of the microlenses.

The overall shape of the fabricated microlenses was analyzed by using a surface profilometer (KLA Tencor P-17) which is based on a stylus-based scanning, using a 2.5 µm stylus tip radius. Excluding from the analysis the set of points affected by the footprint of the stylus (from the ground level, about 45 µm along the vertical axis of the lens), the surface profile of the 2PP microlenses fitted the spherical function with a R-square of 0.998 (**Fig.SI6**). The average height and curvature slightly differ from the model (see **Table I** in the main text) and they respectively are 93 µm (+5%) and 193 µm (-3.5%, **Fig.SI6B**). A deviation of the fabricated surface from the desired spherical one is expected due to the dimensions of the polymerized voxel and some possible shrinking occurring upon developing the microstructure. This deviation can be corrected by working on the CAD shape of the lens and the stability can be improved by increasing the thickness of the 2PP shell by multi-scan, specially for the pedestal which is the weakest part of the lens.

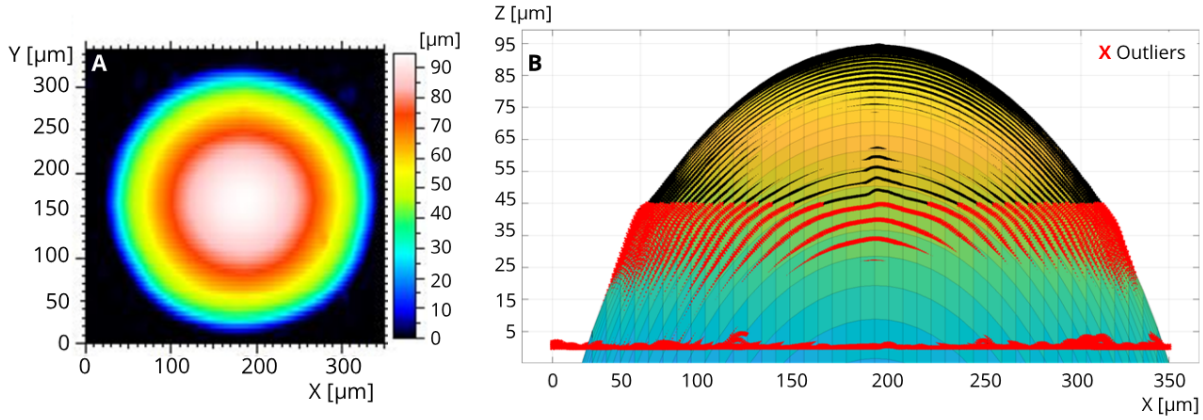

Figure SI6. Outcome from the profilometry measurements. **A**: Height of the overall lens plotted using a color code diagram; **B**: Spherical fitting of the surface profile of the fabricated lenses excluding the data affected by the footprint of the stylus tip of the profilometer (red points).

SI7. Intensity distribution sampling along the optical axis.

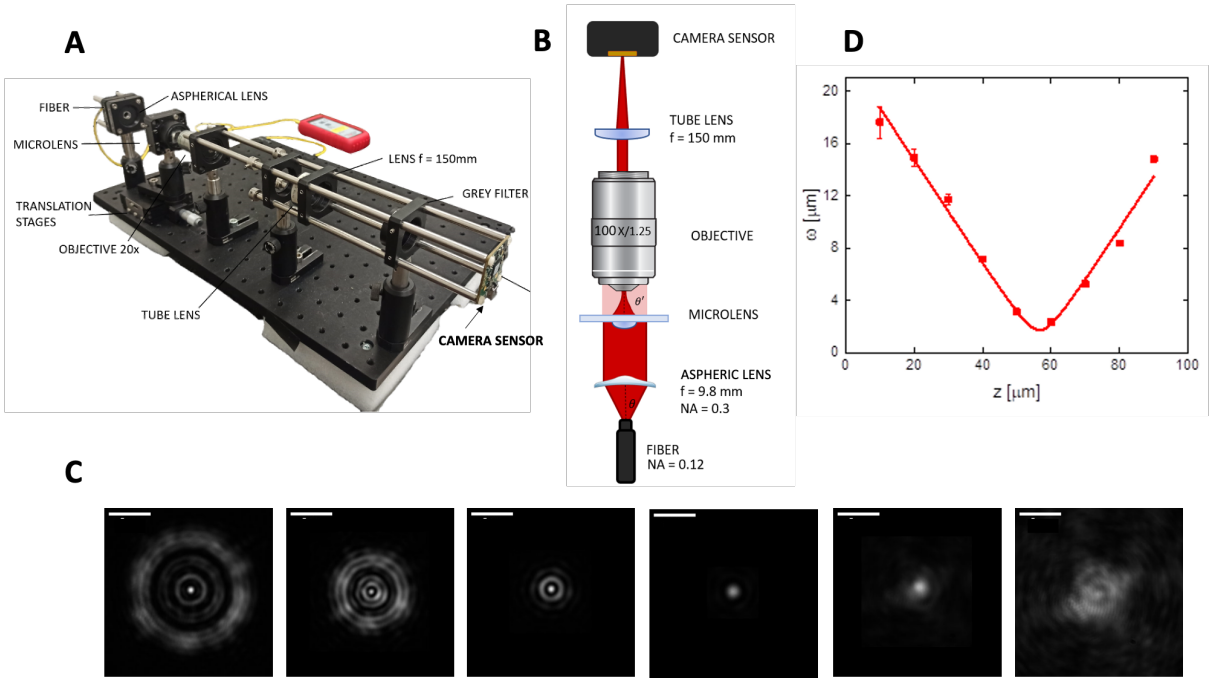

Figure SI7. Minimum Spot Size test. **A**: Photograph of the setup for the test of the minimum beam spot and the Rayleigh range of the microlenses. **B**: Sketch of the optical path. The tube lens and the camera sensor are aligned to accept rays from infinite. **C**: Images of the intensity profiles collected at various distances along the microscope objective optical axis. The mutual distance between the planes is 10 μm, starting from the plane closer to the microlens (from the left to the right). Scale bars 5 μm. **D**: Trend of the effective beam waist measured by the cumulative sum of the intensity profiles in panel **C** fitted to **Eq.SI7.3**. The solid line corresponds to the fit of the effective beam waist data to **Eq.SI7.2**. The best fit values are $w_0 = (2.0 \pm 0.3)\,\mu m$ and $z_R = (5.6 \pm 1.5)\,\mu m$ (average values over a full array of 7 microlenses).

The intensity distribution on planes perpendicular to the optical axis provides a direct visualization of the effect of the spherical aberrations[5]. We have sampled the intensity at $10\,\mu m$ steps by means of an infinite conjugated microscope working at 635 nm (**Fig. SI7**). The tube lens and the camera sensor are aligned to accept rays from infinity. In this way the microscope objective collects the electromagnetic field in its front focal plane (**Fig. SI7A-B**). The images collected by the camera at various positions of the objective focal plane give us the shape of the intensity profile generated by the microlenses. An exemplary set of images is reported in **Fig.SI7C**, evidencing the effect of the spherical aberrations of the microlens.

Due to the presence of the spherical aberrations, a measurement of the value of the $1/e^2$ beam size cannot be directly obtained by fitting the intensity distributions of **Fig.SI7C**. At each plane perpendicular to the optical axis (for each image in **Fig.SI7C**), we can try to obtain an approximate value of the $1/e^2$ beam size by computing and fitting the cumulative sum of the

beam intensity distribution along the columns of the image. In fact, an ideal Gaussian beam is determined by the beam waist, w_0 , and the Rayleigh range, $z_R = \pi w^2{}_0/\lambda$, as:

$$I(x,y,z) = A/w(z)^2\, exp\{-2[(x-x_0)^2-(y-y_0)^2]/w(z)^2\} + B \qquad \text{(SI7.1)}$$

$$w(z) = w_0\sqrt{1+(z/z_R)^2} \qquad \text{(SI7.2)}$$

Given the image of the beam intensity profile, the cumulative sum of the intensity distribution detected along the image columns (here the y axis) is given by ref.[6]:

$$< I(x,z) >_y = A\pi w^2(z)[1-erf(\sqrt{2}(x_0-x)/w(z)] + BMx \qquad \text{(SI7.3)}$$

Here M is the length in pixels of the image columns. By the computation of $< I(x,z) >_y$ for each image in **Fig.SI7C** and its fit to **Eq. SI7.3** we obtain an effective value of the $1/e^2$ beam radius $w(z)$ at each value of the distance, z, along the optical axis. $w(z)$ is plotted as a function of z in **Fig.SI7D**. The best fit values of the beam waist and the Rayleigh range obtained by fitting these data to **Eq. SI7.2** are $w_0 = (2.0 \pm 0.3)\,\mu m$ and $z_R = (5.6 \pm 1.5)\ \mu m$. As a comparison, the value of the Rayleigh range that can be predicted from the beam waist measured from the FWHM on the minimum spot size plane (**Fig.4D** in the main text) is $z_R \simeq (2.5 \pm 1.1)\,\mu m$. The approximate value $z_R = (5.6 \pm 1.5)\ \mu m$ appears therefore overestimated, confirming that the presence of side lobes due to the spherical aberrations in the imaged spot profiles prevent exploiting the Gaussian modeling of the beam. Even the analysis based on the cumulative sum of **Eq. SI7.3** fails in providing an accurate estimate of z_R , that should be measured by the FWHM on the minimum spot size plane as performed in the main text.

BIBLIOGRAPHY

[1] M. F. Griffin, H. E. desJardins-Park, S. Mascharak, M. R. Borrelli, M. T. Longaker, *Dis. Model. Mech.* **2020**, *13*, 1.

[2] F. P. Bolin, L. E. Preuss, R. C. Taylor, R. J. Ference, *Appl. Opt.* **1989**, *28*, 2297.

[3] M. V. Klein, T. E. Furtak, *Optics*, 2nd ed., J. Wiley &Sons, New York, **1991**.

[4] V. Lakshminarayanan, A. Fleck, *J. Mod. Opt.* **2011**, *58*, 545.

[5] M. Born, E. Wolf, *Principles of Optics*, Pergamon Press, **1959**.

[6] M. Bouzin, G. Chirico, L. D'Alfonso, L. Sironi, G. Soavi, G. Cerullo, B. Campanini, M. Collini, *J. Phys. Chem. B* **2013**, *117*, 16405.